OPTIMIZATION OF PROTON THERAPY BY ESTIMATION OF THERAPEUTIC PROTON SPECTRUM AND VERIFICATION OF PROTON RANGE.

By

PERCY NEBAH

Bachelor of Engineering
Carl Von Ossietzky
University of Oldenburg
Niedersachsen, Germany
2014

Submitted to the Faculty of the
Graduate College of the
Oklahoma State University
in partial fulfillment of
the requirements for
the Degree of
Masters of Science
December/2017

OPTIMIZATION OF PROTON THERAPY BY ESTIMATION OF THERAPEUTIC PROTON SPECTRUM AND VERIFICATION OF PROTON RANGE.

Thesis Approved:

Jongmin Cho, Ph.D

Thesis Adviser

Eric Benton, Ph.D.

Stephen McKeever, Ph.D.

Salahuddin Ahmad, Ph.D.

ACKNOWLEDGEMENTS

I would first like to thank my Advisor Dr. Jongmin Cho. His constant motivation and support helped me to learn and improve as a scientist and as a person.

I would like to thank Dr. Ahmad for collaborating with us on the studies we carried out. Dr. Ahmad provided us not only with beam time and a good environment at the University of Oklahoma Health Sciences Center to do our experiments, he was always available and contributing intellectually to the work we carried out.

I would like to extend special gratitude to Dr. McKeever for accepting to join my Stillwater, Oklahoma committee. It is a great honor to have him in my committee. I also went to Dr. McKeever for career advice which helped me in very difficult times.

Special thanks to Dr. Benton for being my mentor throughout my time here at Oklahoma State University. Dr. Benton molded me into a better scientist. As he will always say, “think about the basis, and understand the physics”. Well that saying helped me a countless number of times to rethink my steps, be it in coding or actual experiments and produce better results. Dr. Benton’s nuclear physics expertise were invaluable for my thesis and helped me solve several complex difficulties I ran into. He also went beyond his busy schedules to do major corrections to my written thesis. My initial thesis draft and final thesis are two different documents because of Dr. Benton “thank you”.

I would also like to thank Dr. Yong Chen at the University of Oklahoma Health Sciences Center. He was always willing to go beyond his very busy schedule in the clinic to not only help us setup during our experiments but he also spent time with us while contributing meaningfully to our studies. I will also like to extend my gratitude to our other collaborators at OUHSC Dr. Hosang Jin, and Dr. Michael Prusator.

I would like to thank Adam Coleman. When I first walked into our Lab Adam was seated next to me. I didn’t have to walk to far to get help. His machine learning expertise helped me make breakthrough in my optimization and coding.

Special thanks to Dr. Art Lucas. Dr. Lucas was always open to giving us guidance on the electronic aspects of our research.

And finally I would like to thank my parents, Dr. Bridget Nebah my mom and Dr. Jacob Nebah my dad. Without their moral support, constant motivation, prayers, and blessings I will never be at this stage in my career. My parents were always full of positivity. When I called them maybe to moan about something that was not working out for me, I will always end the call with a smile and full of positivity.

Acknowledgements reflect the views of the author and are not endorsed by committee members or Oklahoma State University.

Name: PERCY FORSUH NEBAH

Date of Degree: DECEMBER, 2017

Title of study: OPTIMIZATION OF PROTON THERAPY BY ESTIMATION OF THERAPEUTIC PROTON SPECTRUM AND VERIFICATION OF PROTON RANGE.

Major Field: MEDICAL PHYSICS

Abstract: The purpose of this work was to contribute meaningfully to the field of proton therapy. We carried out two projects with a common goal to better understand the nuclear physics occurring around the Bragg peak, to better understand and control dose deposition within the Bragg peak. In the first study, we developed a novel method to measure the peak energy of therapeutic proton beams. Activation of an element with multiple proton interaction cross-sections was used to estimate the proton energy spectrum. Three natural copper foils (50 mm × 50 mm × 0.1 mm) were placed at three different depths in a water-equivalent phantom. The phantom was irradiated with either a near-monoenergetic proton beam or 10 cm spread-out-bragg-peak (SOBP) proton beam 15.4 cm and 15.3 cm range respectively. The activated copper foils created progeny radioisotopes: 63Zn, 61Cu, 62Cu and 64Cu, which decayed through positron emissions. Radiation emitted from these radioisotopes were recorded using a time coincidence system comprised of 3 pairs of scintillation detectors. The relative fractions of the radioisotopes were calculated from the recorded time activity curves, using the least-squares fitting. The relative fraction of each radioisotope is proportional to the convolution of its proton-interaction cross-section and the proton energy spectrum. Our optimization code iteratively solved for the best spectrum peak energy, which resulted in the relative fraction of radioisotopes that matched closest with the decoupled radioisotope fractions. A quantitative evaluation comparing our results with Monte Carlo simulations was performed using the Chi-squared method. There was a good agreement between the optimized and simulated spectra (Chi-square of $\alpha = 0.05$ (Level of significance)). In the second study, we developed a novel method for proton range verification. This was based on indirectly detecting Prompt gamma (PG) emitted from a hard water phantom during proton irradiation. High energy PG rays created in a hard water phantom during proton irradiation are intercepted by a lead slab. The PG rays interact by pair production with the nuclei of the lead slab resulting in the production of positron and electron pairs. The positrons rapidly annihilate with the surrounding electrons of the lead slab resulting in the emission of pairs of 511 keV annihilation gamma (AG) rays. The intensity of the AG rays correlates with the intensity of the emitted prompt gamma radiation and was used to determine the range of the proton beam in the phantom. Preliminary results from our method were compared to Monte Carlo simulated results and looked promising. Our system also proved to be ~10 times more sensitive than direct PG detection methods for example, the IBA gamma camera.

Table of Contents

List of Figures

List of Tables

Chapter 1

Introduction

Cancer can be defined as a disease in which a group of abnormal cells grow uncontrollably against the normal rules of cell division. This uncontrolled growth is as a result of the cancer cells developing a degree of autonomy from the signals that dictate whether the cell should divide, differentiate into another cell type or die. This resultant uncontrolled growth and proliferation, if allowed to continue and spread, can be fatal. Cancer is one of the major causes of death especially in the aging population of today. At least one in three people will develop cancer, one in four men and one in five women will die from it (Hayat et al., 2007). This has motivated scientists and researchers to find ways of controlling, treating or, even better, preventing cancer. Radiotherapy is one of the most successful treatment options for cancer, alongside surgery and/or chemotherapy. Radiotherapy uses high doses of radiation to induce damage to the DNA of cancer cells, which ultimately leads to cancer cell death. However, during treatment, healthy organs are also exposed to radiation so, accurate delivery of the treatment dose is vital.

Advances in imaging, treatment planning, and tumor targeting have led to a substantial increase in radiation delivery precision. To date, the most advanced photon treatment delivery method is intensity-modulated radiation therapy (IMRT). IMRT delivers high doses of X-rays to tumor targets while minimizing the dose delivered to normal healthy tissue. High doses to healthy tissue are avoided with IMRT by applying numerous radiation fields of varying intensities from different angles. This requires increasing the volume of irradiated normal tissue. This is a limitation of IMRT because the exposure of more healthy tissue to low doses of radiation can lead to secondary cancers or other unwanted tissue side effects. An alternative treatment modality with decreased exposure of normal healthy tissues is proton beam radiotherapy.

The existence of protons was first demonstrated by Ernest Rutherford in 1911 (Rutherford, 1911). He targeted energetic α particles (He^{2+}) at a foil and measured the deflection as they came out the other side. He found that most of the α particles passed through the foil undisturbed, some were occasionally scattered at large angles and a few bounced back directly towards the source. From these results, Rutherford discovered the nucleus and suggested that the nucleus contained a particle with a positive charge called a proton. Proton research then became very prominent and by 1930 E.O Lawrence built the first cyclotron. In 1946, Robert R. Wilson at Harvard University suggested that energetic protons could be an effective cancer treatment method (Wilson, 1946). In his paper, Wilson explained the biophysical hypothesis for proton therapy, as well as key engineering techniques of beam delivery. Cornelius Tobias and his colleagues at Lawrence Berkeley Laboratory first treated patients with protons in 1955. Interest in proton therapy slowly grew and, given the advantages it presented itself as a comparable modality to a conventional x-ray radiotherapy, by 2017 about 65 facilities worldwide were using proton beams for radiotherapy (particle therapy facilities in operation, www.ptcog.ch, July 2017).

Cancer treatment with protons offers a number of significant advantages over conventional treatment with x-rays or electron beams. Protons penetrating a medium, lose energy through Coulombic and nuclear interactions. Protons of a given energy have a finite and well-

defined range in water and tissue, whereas the range of x-rays is theoretically infinite and poorly defined. The rate of energy loss is most rapid in the last few millimeters of penetration. As protons traverse matter such as a column of water or the body of a patient, their kinetic energy decreases, and the dose deposition rate increases. The kinetic energy of the proton is lowest at the end of its range, while there is a sharp increase in dose deposition, known as the Bragg peak, just before the beam stops. This is followed by a sharp dose falloff distal to the Bragg peak. The penetration depth of the Bragg peak is directly related to the initial energy of the charged particle. For irradiation of a tumor, the proton beam energy and intensity are varied to distribute the Bragg peak over the whole tumor volume.

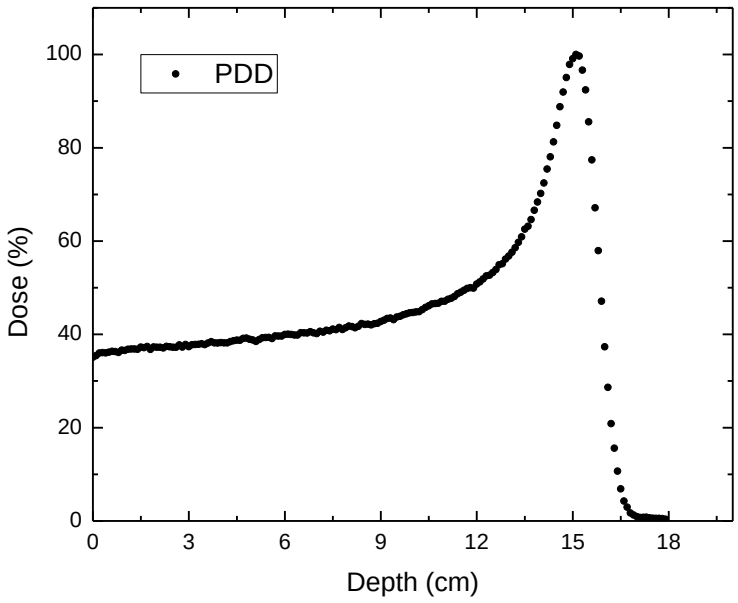

Figure 1.1. Monte Carlo simulated percentage depth dose curve of a monoenergetic proton beam showing a sharp increase or peak in dose called a Bragg peak.

Critical organs and healthy tissue beyond the Bragg peak are spared because of the rapid falloff in dose following the Bragg peak. The accuracy of the position of the Bragg peak is very

crucial during proton therapy. A position uncertainty greater than a few mm can result in the delivery of high doses of radiation to healthy tissue.

The work described in this thesis is meant to contribute meaningfully to the field of proton therapy. We carried out two projects with a common goal to better understand the nuclear physics occurring around the Bragg peak, to better understand and control dose deposition within the Bragg peak. The first project (Chapter 3) introduces a method of determining the peak energy of a proton spectrum at different depths near the depth of the Bragg peak. This method is based on the use of activation products of proton-nucleus (p, x) interactions with natural copper in order to determine the peak energy of the proton spectra for both monoenergetic and Spread Out Bragg Peak (SOBP) proton beams. There are four nuclear reactions possible between energetic protons and the nuclei present in natural Cu that yield a significant number of Annihilation gamma (AG). The maximum cross-section for these reactions is quite different from one another, ranging from less than 50 to 400 mb. Moreover, the maximum cross-section for each of the four nuclear reactions occurs at a different proton energy. By measuring the rate of radioactive decay as a function of this four AG emitting isotopes produced in (p,x) reactions and then deconvolution the resultant curve into separate curves for each radioisotope, we can determine which of the four (p,x) reactions dominated and thereby infer the maximum energy of the proton beams at the location of the copper foil within the phantom. Copper activation foils were placed at several depths within the expectation region of the Bragg peak in a hard water phantom. The phantom was exposed to a radiotherapy proton beam in order to induce activation in the copper foils. The activation foils were removed and 511 keV AG activity from the foils was measured as a function of time. The measured decay curves were then separated into decay curves for each possible AG radioisotope and used together with the nuclear cross-sections for the proton activation of the foils, as input parameters to a minimization algorithm to solve for the proton spectrum peak energy. The resultant spectra from this study were compared with Monte Carlo simulation spectra.

In the second study (Chapter 4), we addressed the problem of the uncertainty in the exact position of the distal edge of the Bragg peak. Protons traversing the patient during treatment activate carbon and oxygen nuclei in the patient, which then decay within a few nanoseconds, emitting high energy gamma rays called *"prompt gammas"* (PG). The proton energy for maximum PG activation occurs within a well-defined, finite, distance from the Bragg peak in water and tissue. By locating the depth of maximum PG production, we can infer the position of the Bragg peak within a phantom or even a patient. Instead of detecting the PG directly, our novel method is based on detecting pairs of AG emitted after these PG radiations interact via pair production with a lead slab. We placed lead slabs adjacent to a tissue equivalent phantom and outside the volume irradiated by the proton beam. A pair of scintillation based gamma ray detectors were positioned on either side of the lead slabs in order to detect coincident pairs of AG produced following pair production of PG in the lead. Since the intensity of the measured AG correlates with the intensity of emitted PG radiation, the measured AG counts can be correlated with the dose deposited by the incident proton beam and thus, can be used to determine the proton range in the medium. A feasibility study was carried out to investigate this approach.

This paper presents the results obtained and a comparison of the results with Monte Carlo simulations. Monte Carlo simulations are typically considered the most reliable method used in the clinic for proton spectrum determination in treatment planning systems and proton range estimations.

Chapter 2

Theoretical Background

2.1 Proton Therapy

The goal of radiotherapy is to maximize the dose to malignant cells while minimizing exposure to healthy cells. The accuracy with which the dose is delivered to the cancerous cells depends on precisely locating the target, accurately aiming the radiation beam, shaping the radiation beam to the target and minimizing patient movement during treatment. The finite range of protons during treatment is an advantage because dose to organs at risk distal to the proton beams are spared.

There are two main types of proton beam delivery systems, passive scattering, and active scanning. A passive scattering beam delivery system uses scatterers and collimators to obtain a large beam with a homogeneous particle distribution. A range shifter is used for modulating the beam energy and hence the penetration depth. Using a patient-specific beam collimator, the beam is tailored to the required shape of the treatment field. In the active scanning beam delivery system, magnets deflect and steer the proton beam onto the target. Under computer control, the beam "paints" the treatment volume voxel by voxel, in successive layers. The depth of the Bragg peak is adjusted by varying the energy of the beam before it enters the nozzle.

The amount of energy loss is a function of the incident proton particle's kinetic energy therefore, when the proton traverses a medium, its energy loss is often quantified as the linear energy transfer (LET). The linear energy transfer of the particle increases exponentially as the particle's energy decreases (Johns and Cunningham, 1983). It has been shown that higher LET produces more cell deaths than does lower LET radiation and is represented by a parameter called relative biological effectiveness (RBE) (Hall et al., 1988). The relative biologic effectiveness (RBE) also increases as LET increases near the end range of the incident proton (Paganetti et al., 2002). RBE is defined as the ratio of a dose of photons to a dose of any other particle to produce the same biological effects like cell killing, tissue damage, and mutations. The change in RBE with depth in a medium has made the task of measuring the biological dose very difficult.

Accurate knowledge of the LET is required to estimate the proton RBE. Estimation of proton RBE remains a challenge since current LET measurement approaches have several drawbacks. Plastic nuclear track detectors (PNTDs) have no sensitivity for mid LET regions (< 5 keV/μm) (Hoffmann et al., 1980), and signal saturation for high fluence (Benton and Frank, 2002). Semiconductor and optically stimulated luminescence detectors have directional dependency and large uncertainties (Sawakuchi et al., 2010). The Monte Carlo simulations are more commonly used to estimate proton spectra and LET (Granville and Sawakuchi, 2015, Paganetti, 1998). The accuracy of Monte Carlo simulated spectra is usually validated by comparing the results with measured dose distributions. However, proton beams with different energy spectra can give rise to very similar dose profiles. If providing uniform physical dose is the only matter of interest, differences in the proton energy spectra are not a major concern. However, biological dose or RBE is affected by these spectral differences. Hence, it is necessary to validate the Monte Carlo simulated proton energy spectra with measured proton energy spectra.

2.2 Passive Scattering Proton Beam Delivery System

Passive scattering is a proton beam delivery system where the cross-sectional area of the proton beam is spread by placing a scattering material in the beam path. It is divided into two types, single scattering, and dual scattering. Single scattering is achieved by placing one scattering material across the path of the protons. This broadens the beam sufficiently for treatment of small fields. Treatment of larger fields requires a second scatterer called dual scattering. Shown in figure 2.1 is a diagram showing the configuration of the beam line components of a dual scattering beam delivery system.

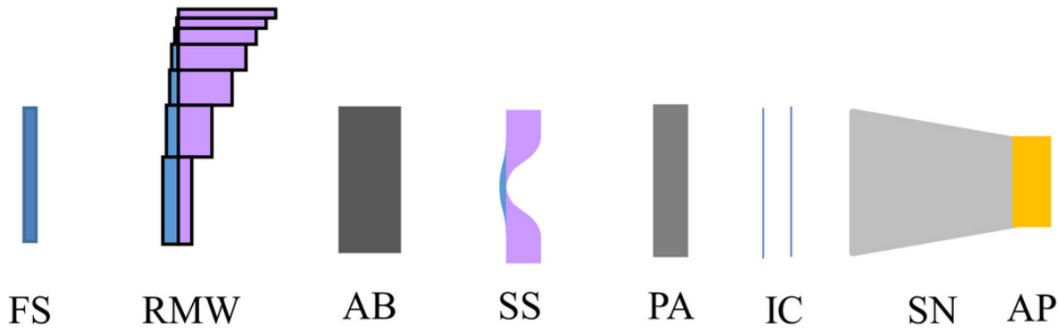

Figure 2.1. FS is the first Scattering foil, RMW is the range modulator wheel, AB is an energy degrader, SS is the second scattering foil, PA is the post absorber, IC is the ion chamber, SN is the snout and AP is the aperture (Prusator et al., 2017).

The proton beam from the cyclotron first passes through a lead first scatterer, introducing an initial beam spread. The beam then passes through a range modulation wheel (RMW) made up of one track of graphite and second track made up of lead to ensure uniform scattering power over all steps of the wheel. A RMW is a rotating wheel with variable thicknesses of low Z materials like graphite or plastic, that reduces the ranges of the monoenergetic beam from the cyclotron to create the desired SOBP. The lead in the RMW helps to ensure uniform broadening of the beam across each step of the wheel. After the RMW is a bilayer contoured scattering foil made of lead

and lexan to introduce a second broadening and flattening of the beam. The beam then goes through a graphite absorber for energy degradation and two ion chambers to monitor the beam output. The experiments in this study were undertaken using the Mevion S250 (Mevion medical systems, Littleton, MA, USA) proton therapy system at the University of Oklahoma Health Science Center. Using a passive dual scatter proton therapy unit delivering a pulsed beam of nominal energy 250 MeV (Prusator et al., 2017).

2.3 Interaction of a Proton Beam with a Medium

A proton beam traversing a medium slows down by undergoing Coulombic or ionization interactions with the atomic electrons in the medium. These interactions are caused by electrostatic forces between the positive charges of the incident protons and the electrons of the stopping medium and result in the protons losing their energy through ionization and excitation of atoms along the particle trajectory in the medium. The energy of the protons if high enough knocks an electron out of an atom creating an electron/ion pair. However, if the energy transferred from the incident particle is not sufficient to eject an electron from the atom, it may raise the electrons to a higher energy level, leaving the atom in an excited state. There is also a possibility of head-on collisions of incident protons with atomic nuclei of the stopping medium, resulting in nuclear reactions. These interactions are divided into two types, elastic and inelastic interactions. In an elastic interaction, the incident proton is scattered off a nucleus of the stopping medium and the target nucleus is left intact, while the total kinetic energy of the interaction is conserved. In inelastic scattering, the characteristics of the target nuclei are changed upon impact with the incident proton, while the total kinetic energy is not conserved. Such collisions result in excited nuclei and the possible emission of secondary protons, neutrons, and α-particles.

2.4 Proton Energy Spectrum changes in a Medium

When a monoenergetic proton beam passes through a homogeneous medium, the proton energy spectrum of the beam changes. The proton beam emanating from the beam delivery nozzle is quasi-monoenergetic and loses energy with every interaction event. Since the stopping power is a function of the proton energy, there are small variations in the energy loss of individual protons, leading to a smearing out of the proton beam energy spectrum. This effect is called range straggling and results in the widening of the initial proton energy spectrum as the beam penetrates to deeper and deeper depths.

2.5 Proton Range Uncertainty in a Medium

The energy loss of individual protons when a proton beam traverses a stopping medium is not continuous. This is because the nature of the proton interactions with the medium is stochastic. The number of collisions required to bring a proton particle to rest within the medium will vary slightly with each particle. This results in some proton particles traveling further than others, leading to what is called range straggling. During proton treatment, the superior dose conformity helps concentrate high dose to the tumor volume while sparing healthy tissue proximal to the tumor. Range straggling increases the uncertainty in dose conformity. Any method that could lead to greater precision in knowing a proton beam range in a patient can be used to improve dose conformity.

In addition to the range straggling, the uncertainty in the range of a proton beam in a patient or phantom could be caused by treatment planning uncertainties or treatment delivery uncertainties. Treatment plans are necessary before a patient begins the radiotherapy treatment program that is delivered over a course of several weeks. Computerized tomography scans of the patient are made and from these, clinicians identify and precisely locate the tumor and develop a treatment plan. The accuracy of a treatment plan can be affected by noise distortions in the CT image, and uncertainty in the density and composition of the patient tissue. Moreover,

uncertainties in the algorithm for the conversion of Hounsfield units in which CT data is recorded into tissue density and proton stopping power ratios could also affect the accuracy of the treatment plans.

Uncertainties in the range of the proton beam can also arise during beam delivery. It is always challenging to replicate the same positioning of the patient during treatment in a way that matches the CT simulation positioning and the patient position when early dose fractions were delivered. Although robotic couches and fiducial markers are used to minimize positioning errors, exact reproduction of the prescribed patient alignment is impossible. Patient weight change, tumor shrinkage, normal tissue swelling and involuntary patient movement contribute to proton beam range uncertainties. To reduce the effect of beam range uncertainty and ensure that the entire tumor receives the prescribed dose, an additional dose margin is added around the target volume. However, this additional margin reduces the advantages of proton therapy because, with an extra margin, healthy tissue beyond the beam range will be irradiated. To address this problem, researchers have been developing means of measuring the proton beam range *in vivo* by detecting secondary emissions created as the beam traverses the patient.

When a proton beam interacts with tissue, several types of secondary emissions occur including: thermoacoustic emission, positron annihilation gammas (AG) and high energy prompt gammas (PG). The incoming proton beam can undergo nuclear interactions with tissue nuclei creating short-lived radioisotopes like Carbon-11 and Oxygen-15 that decay by positron emission. The emitted positrons annihilate with nearby electrons producing pairs of 511 keV AG rays. By detecting the emitted annihilation gamma rays using a positron emission tomography (PET) imaging technique, the proton beam delivery and range can be monitored *in vivo*. These detected AG have been shown to correlate with the range of the proton beam within the patient (Litzenberg et al., 1999, Parodi et al., 2007). The nuclear interaction cross-sections leading to the creation of positron emitting radioisotopes Carbon-11 and oxygen-15 (Nishio et al., 2005, Nishio

et al., 2008), show that the threshold proton energies for these nuclear interactions are approximately 16.6 MeV and 20.3 MeV. Protons of these energies have ranges of 2 mm and 4 mm in water, respectively. Detecting the emitted positrons resulting from the decay of the created radioisotopes can be used to verify the range of the incident proton beam within 2-4 mm uncertainty.

The feasibility of detecting high energy prompt gamma rays emitted during proton irradiation for range verification has been investigated by (Min et al., 2006, Polf et al., 2009). Proton-induced nuclear interaction can leave tissue nuclei in excited states. These nuclei then de-excite to ground state by prompt gamma emission. Studies by (Min et al., 2006, Polf et al., 2009) have shown that the distribution of PG emission correlate with the proton depth dose profile. Prompt gamma emission detection for range verification possesses some advantages compared to PET. In a treatment room where there is no in-beam PET, the patient after treatment delivery must be moved to a to an off-line PET system in a different room. The time delay due to the process of moving the patient results in a substantial loss of AG signal. Furthermore, physiological processes such as blood flow cause diffusion of some of the positron emitters from the treatment area over time. This has a negative effect on the correlation between the delivered dose and the PET image. PG detection for range verification overcomes these drawbacks of PET monitoring. The production cross-section for PG emission is higher near the end-of-range of the proton beam compared to that for producing the positron emitters (Moteabbed et al., 2011). This results in a high PG counting statistics which in turn provides a better correlation with dose and better range verification compared to PET. Prompt gamma rays from activated tissue nuclei are emitted a few nanoseconds following proton nuclear interactions, allowing for *real-time* range verification. This *real-time* feature of PG range verification provides a major advantage in that, range errors can be continuously tracked and corrected during treatment.

Because the emitted PG are of relatively high energy (2 – 15 MeV), *in vivo* detection is very challenging. The current gamma ray detection systems using fast scintillators (Christian et al., 2014, Mauro et al., 2014) and Compton cameras (Hueso-González et al., 2014, Kormoll et al., 2011) for PG imaging have poor detection efficiencies for high energy gamma rays because the Compton interaction probability of these high energy PG rays with the detector crystals is low. There is a fixed correlation between the depth of maximum PG counts and the depth of the Bragg peak. By finding the depth of the maximum PG production, we can infer the depth of the Bragg peak inside the patient, and hence, verify the range of the incident proton beam in the medium.

2.6 Proton Nuclear Interactions and Cross-sections

Inelastic interactions of energetic protons with target nuclei is of great relevance in this study. Inelastic interactions can be divided into two types: *compound nucleus* formation reactions and *direct* reactions. A compound nucleus is formed when an incident particle is absorbed by the target nucleus via nuclear strong forces when it gets close enough during a collision. After absorption, the incident particle's energy is evenly distributed amongst the target's nucleons leaving the compound nucleus in an excited state. The compound nucleus then decays by the emission of one or more secondary particles. This reaction can be written,

$$a + A \rightarrow C^{*} \rightarrow B + b\,, \qquad (2.1)$$

where a is the incident particle, A is the target nuclei, C^{*} the formed compound nucleus which de-excites into B by emitting b (Benton, 2016, Krane, 1988). The probability of a reaction between a and A taking place as a result of the collision is defined as the cross-section. This nuclear reaction probability depends on the target composition and the energy of the incident particle.

Suppose a proton particle passes through a thin target of copper foil. The probability of nuclear interaction (dW) is related to the cross-section (σ) by the following equation (Tavernier, 2010).)

$$dW = dxN\sigma \quad , \qquad (2.2)$$

Where *dx* is the thickness of the copper foil and N is the number of scattering targets per unit volume and is determined from the equation:

$$N = N_A \frac{\rho}{A_W} \quad , \qquad (2.3)$$

where, N_A = 6.025x10^{23}, A_W = atomic weight and ρ is the density of the target medium.

The probability of a nuclear interaction *dW* can be defined as the ratio of detected events N_{events} to the number of incident particles $N_{Incident}$,

$$dW = \frac{N_{events}}{N_{incident}} \quad , \qquad (2.4)$$

From equations 2.2, 2.3 and 2.4, the cross-section for a nuclear interaction is defined as,

$$\sigma = \frac{N_{events}}{N_{incident}} \frac{A_W}{dx \rho N_A} \quad . \qquad (2.5)$$

Direct reactions, unlike compound nucleus formation reactions, are a one-step process. The incident particle may undergo one of three reactions with the target nuclei: 1) inelastic reactions, 2) knock-out reactions, and 3) stripping/pickup reactions (Benton, 2016).

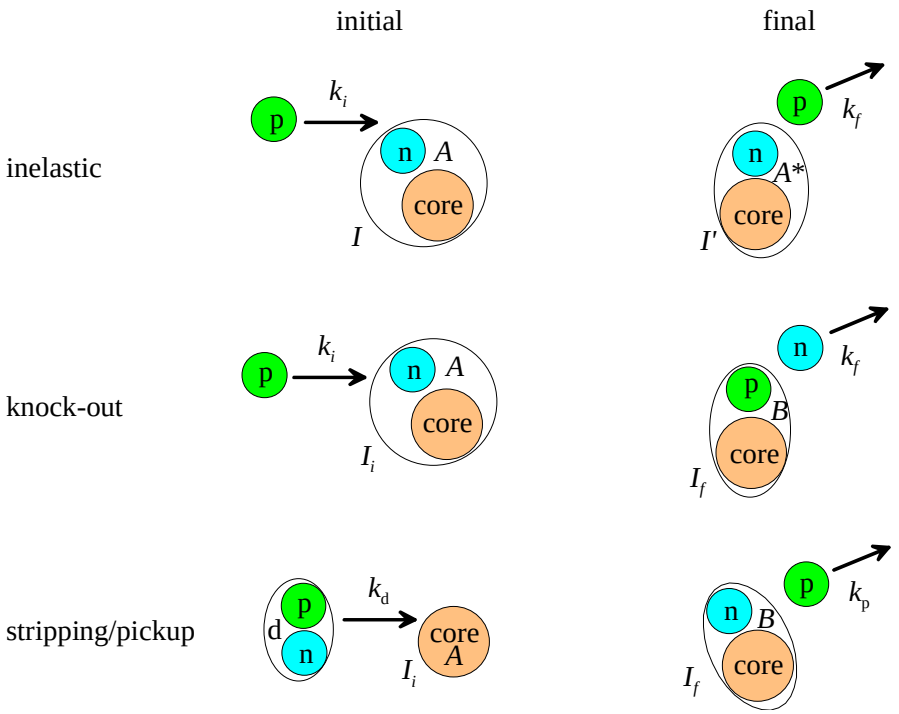

Figure 2.2. Three types of Direct reactions: inelastic (top), knock-out (middle), and stripping/pickup(bottom) (Benton E. 2016).

As shown in figure 2.2, in the inelastic reaction linear momentum, angular momentum and kinetic energy are transferred between the incident particle and target, leaving the target nucleus in an excited state. In the case of a knockout reaction, the incident particle, after a collision with the target nucleus, knocks out one or more nucleons from the target. For example, a ${}^{Z}_{A}X(p,2p){}^{Z-1}_{f}X$ reaction is a knock-out reaction where an incident proton knocks two protons out of the target nuclei. In the stripping reaction shown in figure 2.2, a neutron is stripped off an incident deuteron by the target leaving a proton. The opposite could also happen where the incident projectile can pick up a nucleon from the target in a reaction called a pickup reaction. High energy protons incident on a copper foil activates the foil via any of the above reactions.

2.7 Pair Production and Annihilation Gammas

Pair production usually occurs when a photon of energy greater than 1.022 MeV interacts with the electromagnetic field of a nearby heavy nucleus. The energy of the incident photon is converted into matter through the creation of a negative electron (e^-) and a positron (e^+) pair. A minimum energy of 1.022 MeV is required to create this pair because the rest mass energy of the electron is 0.511 MeV and a pair of oppositely charged electrons, needs to be created in order to conserve electric charge and lepton number. Pair production can only occur in the vicinity of a massive object (e.g. heavy nucleus) for both energy and linear momentum to be conserved.

If a photon of energy 4.44 MeV undergoes pair production, kinetic energy of (4.44 - 1.022=3.416) MeV is transferred to the created electron-positron pair. Due to the conservation of momentum, both particles will tend to be emitted in the forward direction relative to that of the incident photon. The emitted positron after pair production can interact with matter of the stopping medium through ionization, excitation, and Bremsstrahlung, until it loses most of its kinetic energy and slows down. When the positron slows down sufficiently, it will collide with an electron, resulting in an annihilation reaction and the creation of a pair of 511 keV gamma rays. These two photons are ejected in opposite directions in order to conserve linear momentum.

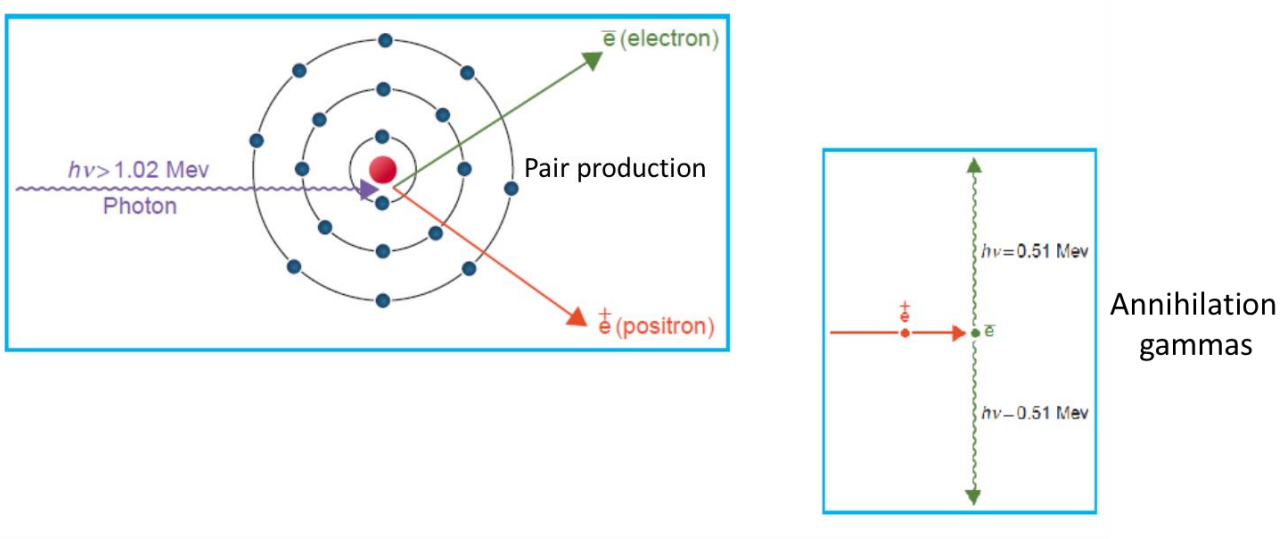

Figure 2.3. Diagram showing pair production (left) and annihilation gamma production (right) (Khan and Gibbons, 2014).

Chapter 3

This chapter documents a study we carried out on the feasibility of using proton activation to determine the peak energy of the proton energy spectrum of a passive scatter proton beam. We based our investigation on the creation of radioisotopes upon activation of naturally occurring copper with therapeutic proton beams. Some of these radioisotopes subsequently decay by positron emission. The generation of each radioisotope is dependent on the proton energy and the nuclear cross-section of the specific nuclear interaction. (Cho et al., 2013) used this dependence to determine the elemental composition of tissues irradiated by proton beams. Proton beams of different spectrum created multiple radioisotopes in different proportions. In this study, we investigated the use of activation products of proton-nuclear (p, x) interaction with natural copper in order to determine the peak proton energy for both monoenergetic and SOBP proton beams.

3.1 Proton Activation of Copper

Activation of natural copper with a proton beam can lead to the creation of four radioisotopes: ^{63}Zn, ^{61}Cu, ^{62}Cu and ^{64}Cu. ^{63}Zn decays by positron emission 92.7% of the time and also decays by electron capture 7% of the time. ^{61}Cu decays 61% through positron emission and 39% through electron capture. ^{62}Cu decays via positron emission 97.83% of the time and the rest by electron capture, while ^{64}Cu decays 17.6% by positron emission, 43.5% by electron capture and 38.5% through β^- emission. Table 3.1 shows the reactions leading to the creation of these radioisotope.

Table 3.1 Proton interaction reaction, branching ratio and half-life of positron emitting progeny radioisotopes of natural copper activated by protons.

Element	Proton-element interaction reactions	Branching ratio	Half-life of progeny radioisotope (hrs)
^{63}Cu	$^{63}Cu(p,n)\,^{63}Zn$	92.7	0.641
^{63}Cu, ^{65}Cu	$^{63}Cu(p,p2n)\,^{61}Cu$ + $^{65}Cu(p,p4n)\,^{61}Cu$	61	3.33
^{63}Cu, ^{65}Cu	$^{63}Cu(p,pn)\,^{62}Cu$ + $^{65}Cu(p,p3n)\,^{62}Cu$	97.83	0.161
^{65}Cu	$^{65}Cu(p,pn)\,^{64}Cu$	17.6	12.707

The branching ratios shown in column two are for the positron decays. The measured cross-sections for these reactions were obtained from the Evaluated Nuclear Data library (END) (Chadwick et al., 2006). Each cross-section was multiplied by both the natural abundance of each isotope (63Cu: 69 %, 65Cu: 31 %) and the positron emission branching ratio to create the positron-emission cross-section shown in figure 3.1.

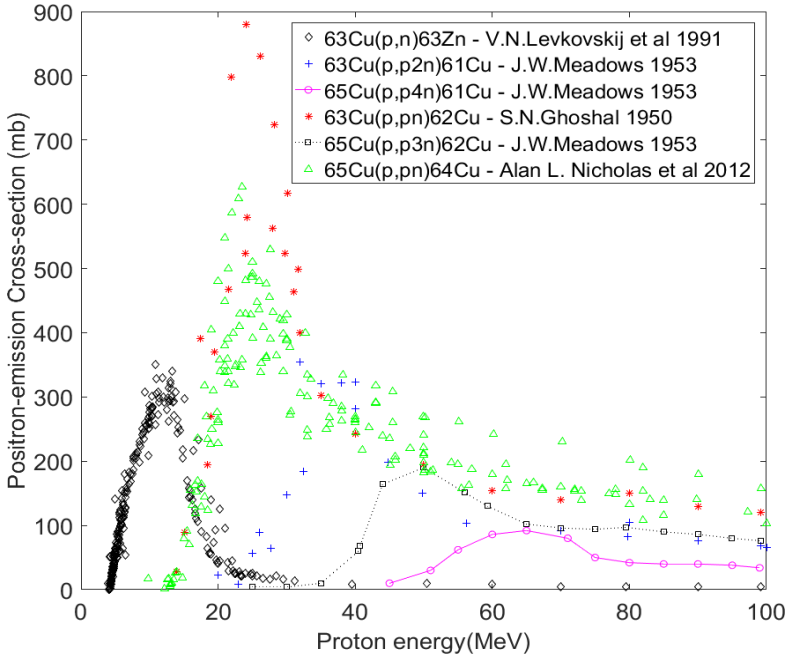

Figure 3.1. Nuclear cross-sections leading to positron emission for copper activated by protons.(Ghoshal, 1950, Meadows, 1953, Nichols et al., 2012, Levkovskij, 1991)

We combined those cross-sections with the same progeny radioisotope. The combined cross-sections were smoothed using a Matlab “boxcar” filter with a span of 0.1 MeV. This resulted in the combined positron-emission nuclear cross-section per progeny radioisotope as shown in figure 3.2.

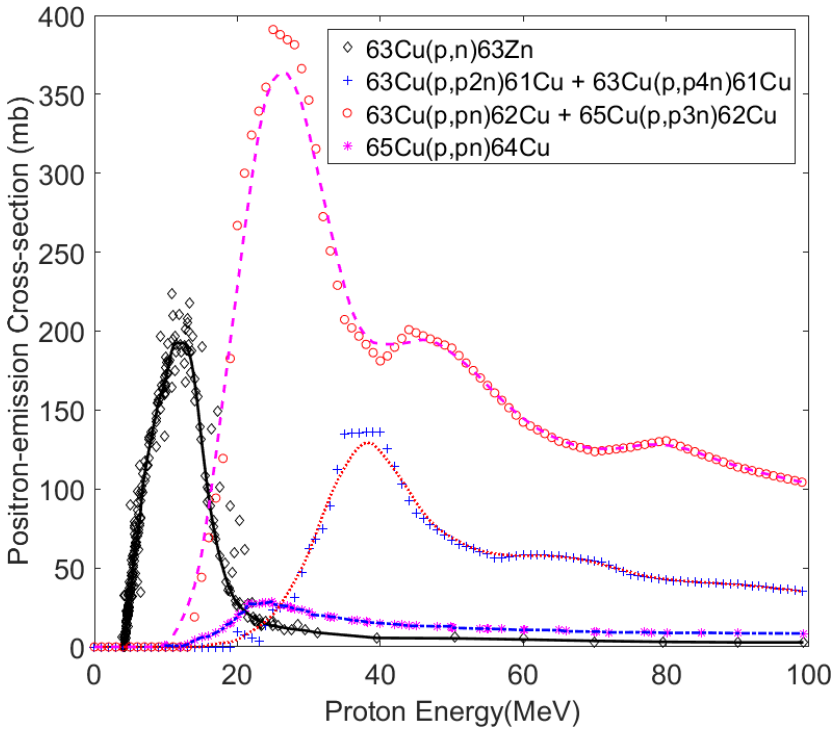

Figure 3.2. Combined nuclear cross-sections in figure 3.1 for each progeny radioisotope. The combined cross-sections were smoothed using a Matlab "boxcar" filter with a span of 0.1 MeV.

3.2 Overlap Region of the Spectrum and Nuclear Cross-section

The fraction of each progeny radioisotope created after activation of the copper foil is dependent on the cross-section, the thickness of the foil and the spectrum of the proton beam bombarding it. If copper foils are sandwiched at some depth in a hard water phantom, as a proton beam traverses the phantom, the energy degrades and when the beam reaches the foil the spectrum shape and peak energy changes. Moreover, as the beam energy degrades, it creates ^{63}Zn, ^{61}Cu, ^{62}Cu, and ^{64}Cu in proportion to the energy dependence of the weighted cross-section for each reaction. The activity of each created radioisotope, *i*, *j*, *k*, and *l* is represented as A(*i*), A(*j*), A(*k*) and A(*l*), respectively. The activity of each radioisotope produced for a given proton energy *E*, can be written as the product of its cross-section and the fluence of protons of energy *E*. Over the whole of the proton energy spectrum, this can be written in matrix form as:

$$\begin{pmatrix} A(i) \\ A(j) \\ A(k) \\ A(l) \\ ... \\ ... \end{pmatrix} = \alpha \begin{pmatrix} \sigma(E\min) & \sigma(E\min+1).....\sigma(E\max) \\ \sigma(E\min) & \sigma(E\min+1).....\sigma(E\max) \\ \sigma(E\min) & \sigma(E\min+1).....\sigma(E\max) \\ \sigma(E\min) & \sigma(E\min+1).....\sigma(E\max) \end{pmatrix} * \begin{pmatrix} \phi(E\min) \\ \phi(E\min+1) \\ \phi(E\min+2) \\ ... \\ ... \\ \phi(E\max) \end{pmatrix}, \quad (3.1)$$

where α is the proportional constant, $\sigma(E)$ is the weighted cross-section for the production of each individual radioisotope and $\phi(E)$ is the proton beam energy fluence activating the copper foil. For example, ^{63}Zn is found to be: $^{63}Zn = \alpha \int_{E\min}^{E\max} {}^{63}Cu(p,n)\,{}^{63}Zn\;\phi(E)\,dE$.

The above is an inverse matrix equation where A and σ are known parameters, while ϕ is an unknown parameter. The method that was used to determine the relative activity (A) of each individual radioisotope is explained in a later section. Using published cross-section data, we can start from a pre-optimized monoenergetic or SOBP proton spectrum and numerically solve equation (3.1) iteratively using an optimization algorithm until we get values sufficiently close to the measured relative fractions of radioisotopes. The peak energy of the proton spectrum for which the difference between the measured relative fraction of each radioisotope and the solution of equation (3.1) is minimum can be taken as the peak energy of the proton energy spectrum at the depth of the Cu activation foil.

3.3 Monte Carlo Simulation

Monte Carlo simulations for this study were provided by (Cho, 2017) and were used as a comparison with our measured peak energy. The monoenergetic and SOBP proton spectra were simulated using TOPAS (Tool for Particle Simulation), based on a GEANT 4 radiation transport Monte Carlo toolkit (Agostinelli et al., 2003). The beamline geometry was based on blueprints of the Mevion S250 proton gantry and nozzle at the University of Oklahoma Health Sciences Center (Prusator et al., 2017). Two phase space files were created according to the blueprints. A 15.4 cm

range (90% dose) monoenergetic beam and a 15.3 cm range 10 cm SOBP beam both 18 cm beam diameter at ISO, were irradiated on a 40 x 40 x 40 cm water phantom and their proton spectrum was scored at 1 mm intervals along the beam direction. More than 1 million histories were run so that the error bars in the dose/depth profiles were less than 1%. The following physics models were used for simulations - g4em-standard_opt3, g4h-phy_QGSP_BIC_HP, g4decay, g4ion-binarycascade, g4h-elastic_HP, g4q-stopping, and g4radioactivedecay with the cut off range of 0.1 mm. Shown below is a graph of the MC simulated monoenergetic spectra at three different depths, 0 cm, 10 cm and 14 cm in a water phantom.

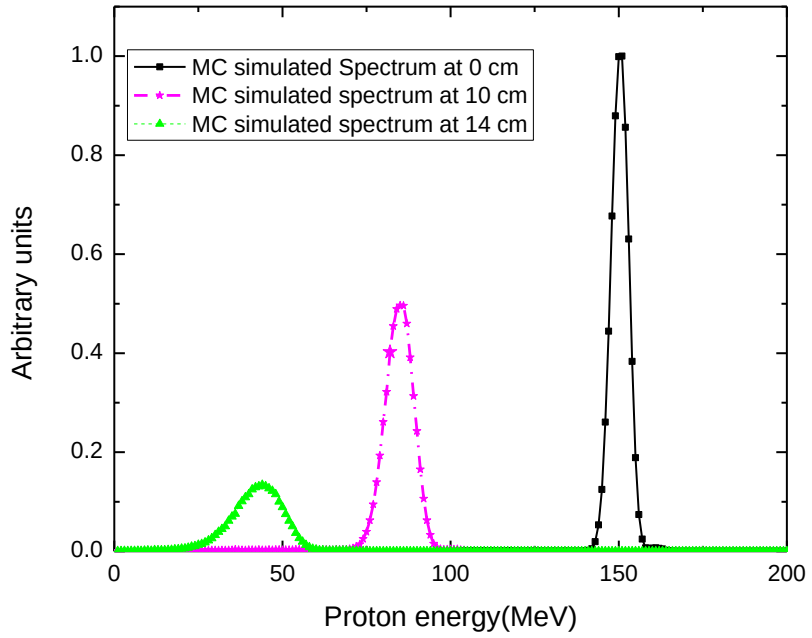

Figure 3.3. Monte Carlo simulated monoenergetic proton spectra at depths of 0 cm, 10 cm and 14 cm in a water phantom.

3.4 Parameterized Monoenergetic Proton Spectra

The proton spectrum exiting the proton accelerator nozzle was assumed to be quasi-monoenergetic with a 2.5% standard deviation of the peak energy and will be referred to as the pre-optimized spectrum. The shape of the spectrum was represented mathematically as a Gaussian distribution using a model developed by (Fourkal et al., 2007). Fourkal derived a power law approximation for the Bethe- Bloch expression (Brice, 1985).

$$\bar{\varepsilon}^{1.715} = \bar{\varepsilon}_0^{\,1.715} + \bar{x} \quad , \qquad (3.2)$$

and

$$\phi(x,\varepsilon) = \phi_0((\bar{\varepsilon}^{1.715} + x)^{1/1.715}) \frac{\bar{\varepsilon}^{0.715}}{(\bar{\varepsilon}^{1.715} + x)^{0.417}} , \qquad (3.3)$$

where ε is the kinetic energy of the protons along their propagation direction, $\bar{\varepsilon} = \frac{\varepsilon}{mc}$, $\phi(x,\varepsilon)$ is the proton energy distribution function, $\bar{x} = \eta x$ is the depth in a medium, and $\eta = 15\eta_e / (m_e c^2) e^4 / (4\pi\varepsilon_0 m_p c^2)$. The numerical value of η for water is 0.002718.

If the initial proton energy spectrum distribution $\phi_0(\varepsilon_0)$ is represented as a Gaussian distribution, the pre-optimized monoenergetic energy spectrum at any depth *x* can be calculated by equation (3.4):

$$\phi(x,\varepsilon) = (\frac{1}{\sqrt{\pi}\Delta} e^{\frac{-(\bar{\varepsilon}^{1.715} - \varepsilon_0)^2}{\Delta^2}}) \frac{\bar{\varepsilon}^{0.715}}{(\bar{\varepsilon}^{1.715} + x)^{0.417}} , \qquad (3.4)$$

where ε_0 is the initial energy of the proton beam and Δ the initial FWHM of the proton spectrum (3 MeV) exiting the beam nozzle. This equation yields broadening and a decrease in amplitude (fluence) of the proton energy spectrum for increasing depth in the stopping medium. Figure 3.4 shows the monoenergetic spectra at varying depths (i.e., 0, 10 and 14 cm) calculated using this method.

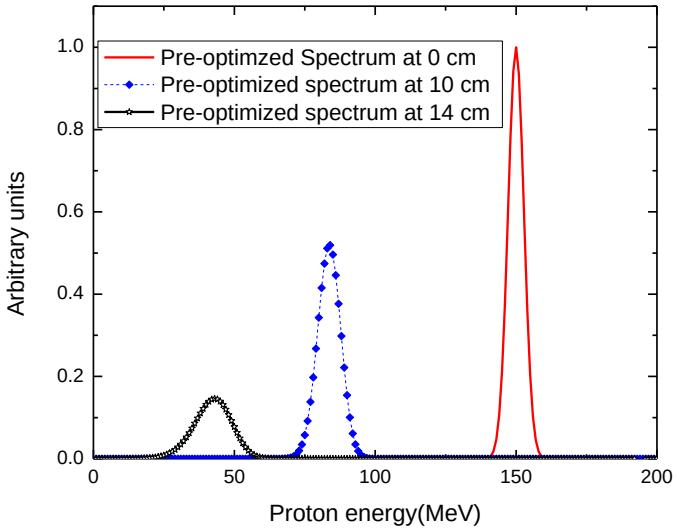

Figure 3.4. Monoenergetic proton energy distribution at depths of 0 cm, 10 cm and 14 cm. In these profiles, we see the widening and reshaping of the initial spectrum with depth.

3.5 Parametrized SOBP Spectra Estimation

A spread out Bragg Peak is obtained by superposition of several monoenergetic proton beams of different initial energy. In the clinic, SOBP beams are generated by employing a monoenergetic beam with high enough energy and range to cover the distal end of the target volume and adding decreasing energy beams to cover the proximal portion of the target volume. The decreasing energy beams are obtained by placing a range modulator across the path of the beam. The modulator degrades the energy of the incident proton beam to the required energy. The SOBP spectra is hence a superposition of several monoenergetic spectra of different energies. Fourkal derived weighting functions for each monoenergetic spectrum which were used to model the pre-optimized SOBP spectrum for this study.

Fourkal derived these weighting functions by using the continuous slowdown approximation (CSDA) to simplify the Boltzmann kinetic equation for protons traversing a medium (Fourkal et al., 2007). The retarding force acting on the protons in the CSDA is the linear collisional stopping power. Neglecting proton nuclear interactions in water, and also neglecting

shell and density corrections, Fourkal determined weights for each Bragg peak used to generate an SOBP dose distribution:

$$W_{mono}(\varepsilon,\delta) = [(\varepsilon_{\max}^2 - (\varepsilon - \frac{\delta}{2})^2)^{\mu} - (\varepsilon_{\max}^2 - (\varepsilon + \frac{\delta}{2})^2)^{\mu})],\ for\ \varepsilon_{\min} \le \varepsilon < \varepsilon_{\max},$$

and

$$W_{mono}(\varepsilon,\delta) = [(\varepsilon_{\max}^2 - (\varepsilon - \frac{\delta}{2})^2)^{\mu},\ for\ \varepsilon = \varepsilon_{\max} \tag{3.5}$$

where, δ is the energy bin width of each Bragg curve, $\varepsilon_{\max}$ = 150 MeV, $\varepsilon_{\min}$ = 5 MeV, μ = 0.43 and $W_{mono}(\varepsilon,\delta)$ are the weights for a monoenergetic spectrum of energy ε. Each monoenergetic spectrum was multiplied by the calculated weights above and summed together as shown in figure 3.5.

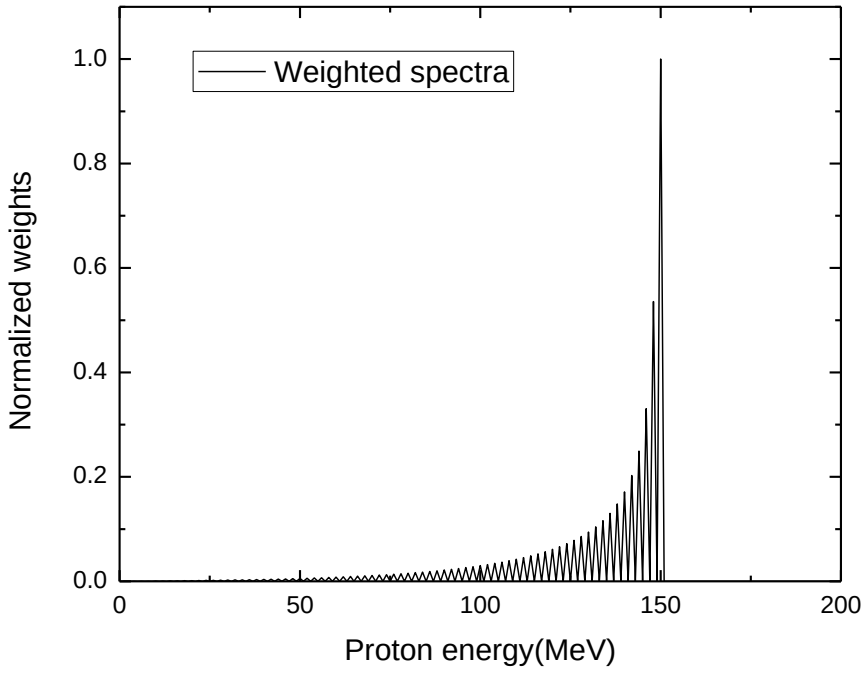

Figure 3.5. Sum of weighted spectra for a 150 MeV SOBP beam at a depth of 0 cm. Each individual spectrum with a 2.5 % standard deviation is weighted with a sampling size δ = 5 MeV.

Each calculated weight represents the magnitude of each monoenergetic spectrum that has been superimposed to generate an SOBP spectrum. The convolution of this summed spectra with the Gaussian distribution:

$$x = \lim_{\Delta \to 0} \frac{1}{\sqrt{\pi}\Delta} e^{\frac{-(\varepsilon_i - \varepsilon_0)^2}{\Delta^2}} \quad , \qquad (3.6)$$

yields the 10 cm SOBP spectrum used in this research shown in figure 3.6.

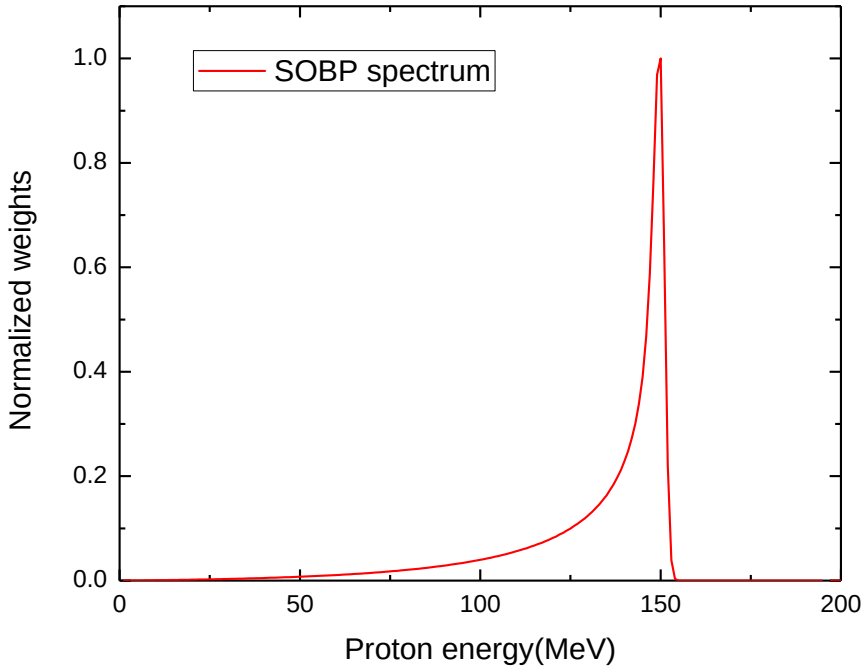

Figure 3.6. The 10 cm SOBP spectrum resulting from the convolution of the sum of the weighted spectra and a Gaussian distribution.

The spread, Δ, in the Gaussian distribution in equation (3.6) was estimated by (Fourkal et al., 2007) to have a threshold value related to the parameter, $\frac{\delta}{\Delta} = 1.7$, where δ is the energy bin width of each Bragg curve in equation (3.5). In this study, the 150 MeV SOBP spectrum was generated by superposition of 15 monoenergetic spectra, each with a bin energy width δ = 10 MeV. CSDA accounted for the change in the shape of each individual spectrum with an increasing depth in

water. Using this method, we generated the 10 cm SOBP energy spectra for different proton ranges in water as shown in figure 3.7.

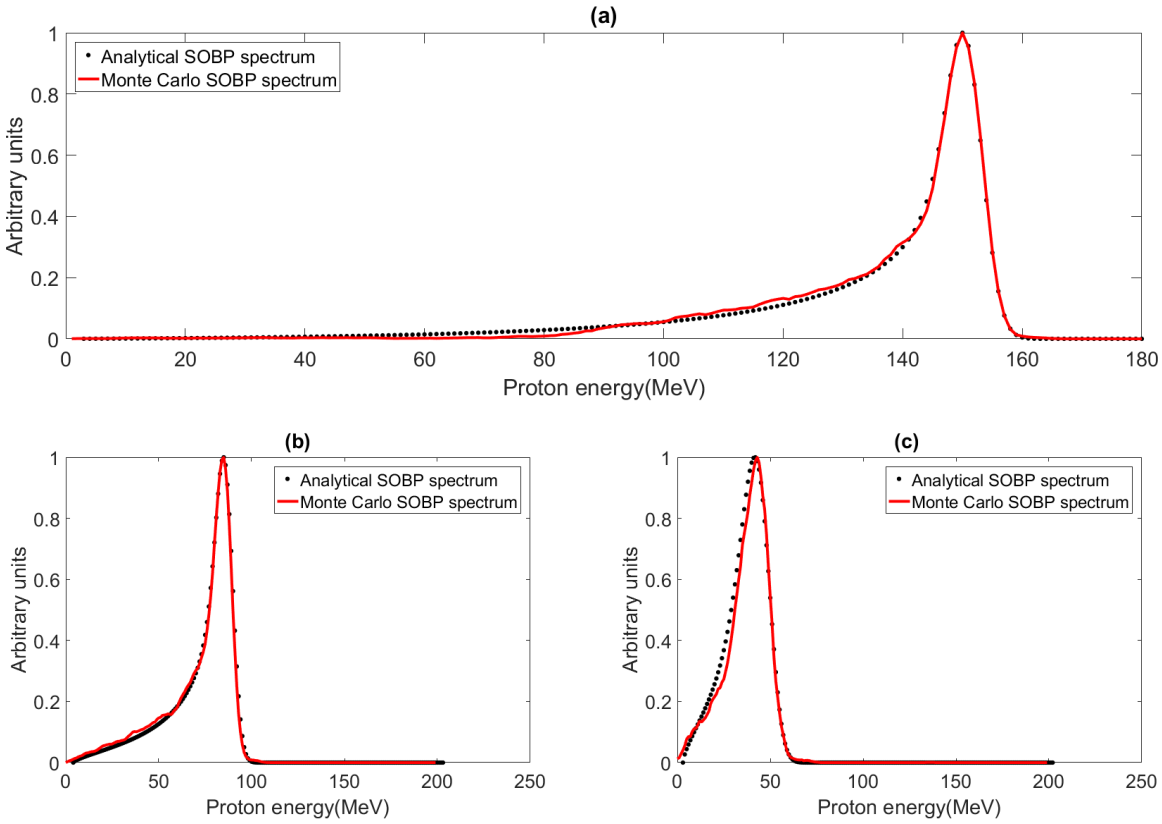

Figure 3.7.Analytical calculated proton energy SOBP spectrum with initial energy 150 MeV compared with the simulated Monte Carlo spectrum. a) and b) represent the spectrum for depths of 0 cm and 10 cm respectively. c) Shows the initial spectra at a depth of 14 cm. Convolution was performed with a Gaussian spread, $\Delta = 5$ MeV and energy sampling interval, δ =10 MeV.

3.6 Materials and Methods

3.6.1 Experimental Setup and Procedure

The feasibility experiments to test this approach of determining the peak proton energy at a given depth in a phantom were carried out at the Stephenson Cancer Center, University of Oklahoma Health Science Center proton therapy facility. Three copper foils, of 50 mm × 50 mm × 0.1 mm each, were sandwiched at three separate depths 14.0 cm, 15.0 cm, and 15.3 cm in a water equivalent plastic phantom. The phantom was irradiated with a 15.4 cm range (90 % dose) and 2 cm modulation proton beam of peak energy approximately 150 MeV. A second set of foils was irradiated with a 15.3 cm range (90 % dose) 10 cm SOBP proton beam of energy 150 MeV. Both monoenergetic and SOBP beams had an 18 cm beam diameter at the isocenter.

After irradiation, the three foils were removed from the phantom and each sandwiched between three pairs of scintillation detectors. The foils were placed at 1cm from the detector to minimize pulse pile up and maximize the geometric efficiency as the AG rays emanating from the foils were measured. These AG were detected using three sets of time coincidence gamma-ray detectors. A pair of NaI-1.5PX scintillation detectors with (38 mm x 38 mm) crystals and LBR 1PX/1.5-IV scintillation detectors with crystal dimension (25.4 mm x 25.4 mm) were used in this research. These scintillation detectors were all produced by Rexon Inc. (Rexon Inc., Beachwood, Ohio, USA). The fast rise and decay times of our scintillation detectors (230 ns (NaI) and 3.5 ns (LaBr)) increased our peak detection accuracy for our time activity measurements by reducing pulse pile up.

The signals from the photomultiplier tubes (PMT) were sent to an NI PXIe 5160 high-speed digitizer (HSD) driven by an Ni scope instrument driver (National Instruments, Austin, Texas, USA). This digitizer had a speed of 2.5GS/s which reduced the loss of useful gamma-ray signal and increased the efficiency of our system.

The measured decay of 511 keV gamma-rays was used to generate a time activity curve (TAC). The measured TAC were separated into four exponential curves, one for each radioisotope (^{63}Zn, ^{62}Cu, ^{61}Cu, and ^{62}Cu) through an iterative deconvolution method as shown in section 3.6.2.

3.6.2 Determination of the Relative Abundances of Progeny Radioisotopes

The measured decay curves for the copper foils at each depth, 14 cm, 15 cm, and 15.3 cm, were separated into the decay curves for the four radioisotopes ^{63}Zn, ^{61}Cu, ^{62}Cu and ^{64}Cu using equation (3.7).

$$Activated\ Cu = \alpha e^{-\lambda_{63}Zn \times t} + \beta e^{-\lambda_{61}Cu \times t} + \gamma e^{-\lambda_{62}Cu \times t} + \delta e^{-\lambda_{64}Cu \times t} \quad (3.7)$$

Where $\alpha, \beta, \gamma, \delta$ are the relative fractions of the progeny radioisotopes, λ_{Zn63}, λ_{Cu61}, λ_{Cu62}, and λ_{Cu64} are the decay constants of the progeny radioisotope. $\alpha, \beta, \gamma, \delta$ are determined as the best-fit parameters when the measured TAC curves are fitted to equation (3.7) using the non-linear least-square method (Huang et al., 1982). The measured TAC curve was fitted using the Matlab nonlinear least square solver *Isqcurvefit.* The solver started with initial values for parameters $\alpha, \beta, \gamma, \delta$ and iteratively solved for the best values of these parameters which resulted in a better fit of the nonlinear function in equation (3.7) to the measured TAC data. This yielded a TAC curve for each of the four progeny radioisotopes.

3.6.3 Iterative Method of Calculating the Proton Spectrum Peak Energy

The relative fraction of each progeny radioisotope obtained using the method described above was used as an input for an optimization code to determine the proton spectrum peak energy. This code ran using the Matlab minimization algorithm, *"Fminsearch*". *Fminsearch* is an unconstrained nonlinear programming solver that searches for the minimum of an objective function say *f(x).* An objective function is a function the optimization solvers, for example, *Fminsearch* attempt to minimize. An array of initial values *x* is input into *Fminsearch* and the

optimization tool uses this array as a set of initial estimates to find the local minimum of the function. In order to optimize the parameterized monoenergetic spectra, the objective function, *f*, below was minimized.

$$f = (A(i) - \sum \sigma_i(E) \times \phi_i(E))^2 + (A(j) - \sum \sigma_j(E) \times \phi_j(E))^2 + (A(k) - \sum \sigma_k(E) \times \phi_k(E))^2 + (A(l) - \sum \sigma_l(E) \times \phi_l(E))^2 \quad (3.8)$$

where *A* is the relative activity of each measured isotope, $\sigma(E)$ is the nuclear interaction cross-section and $\phi(E)$ is the pre-optimized monoenergetic spectrum, as found in section 3.4 for each radioisotopes *i*, *j*, *k* and *l*. The goal of the optimization code is to obtain a reasonably good guess of the peak energy of the monoenergetic spectrum for which the objective function *f* above is minimum. This resulted in an optimum value of the peak energy of the monoenergetic proton spectrum, at the depth of the Cu activation foil.

For the SOBP case, the Gaussian distribution was replaced by the pre-optimized SOBP spectrum determined in section 3.5.

$$y = (A(i) - \sum \sigma_i(E) \times SOBP)^2 + (A(j) - \sum \sigma_j(E) \times SOBP)^2 + (A(k) - \sum \sigma_k(E) \times SOBP)^2 + (A(l) - \sum \sigma_l(E) \times SOBP)^2 \quad (3.9)$$

An initial array of the peak energy values was used as an initial estimate to find the local minimum of the objective function *y*. Using *Fminsearch*, the peak energy values were iteratively varied until a minimum value *f*or *y* was obtained. This resulted in the best position of the pre-optimized SOBP spectrum peak energy on the energy axis.

3.7 Results

3.7.1 Time Activity Curves

Figure 3.8 (a) shows time activity curves measured after the activation of the copper foils using a 15.4 cm range monoenergetic beam at depths of 14 cm, 15 cm, and 15.3 cm. This TAC curve was determined using a bin size of 1 min. The measured TAC was corrected for the decay of activated Cu that took place during irradiation and before AG counting (Cherry et al., 2012). The post-irradiation delay was (1 min 22 sec) and radioisotope decay during proton irradiation was (9 min 13 sec). Figure 3.8 (b) below shows time activity curves measured after the activation of the copper foils using a 15.3 cm range SOBP beam at depths of 14 cm, 15 cm, and 15.3 cm. The TAC curves were also determined using a bin size of 1 min. The post-irradiation delay (1 min 30 sec) and radioisotope decay during activation time (15 min) were accounted for to estimate the initial activity of each created isotope.

a)

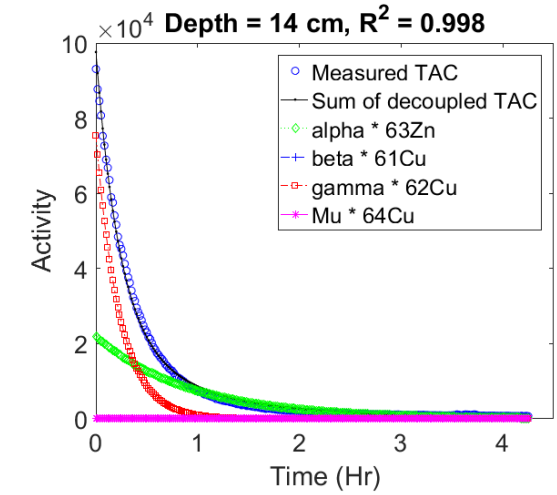
×10^4
Depth = 14 cm, R^2 = 0.998
Measured TAC
Sum of decoupled TAC
alpha * 63Zn
beta * 61Cu
gamma * 62Cu
Mu * 64Cu
Activity
Time (Hr)

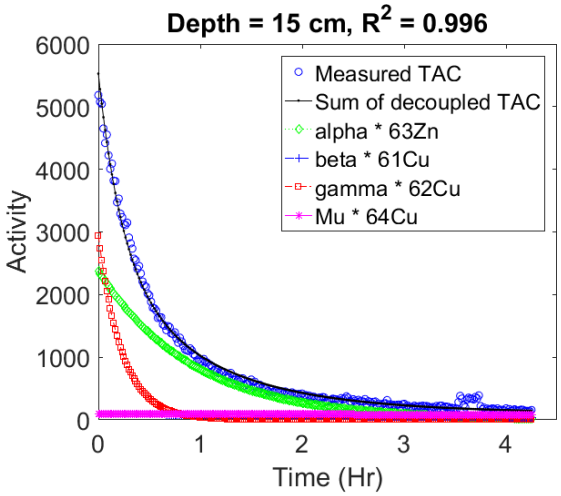
Depth = 15 cm, R^2 = 0.996
Measured TAC
Sum of decoupled TAC
alpha * 63Zn
beta * 61Cu
gamma * 62Cu
Mu * 64Cu
Activity
Time (Hr)

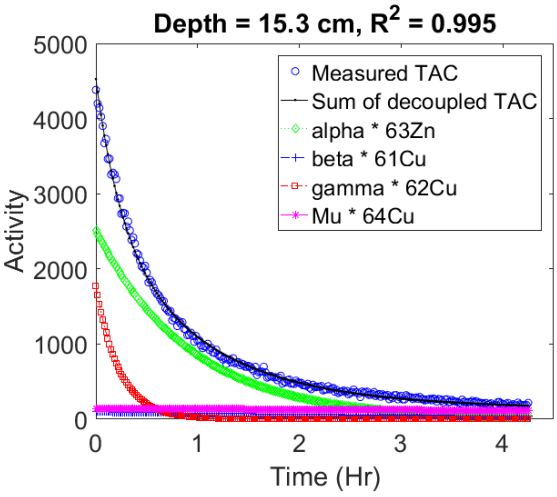
Depth = 15.3 cm, R^2 = 0.995
Measured TAC
Sum of decoupled TAC
alpha * 63Zn
beta * 61Cu
gamma * 62Cu
Mu * 64Cu
Activity
Time (Hr)

b)

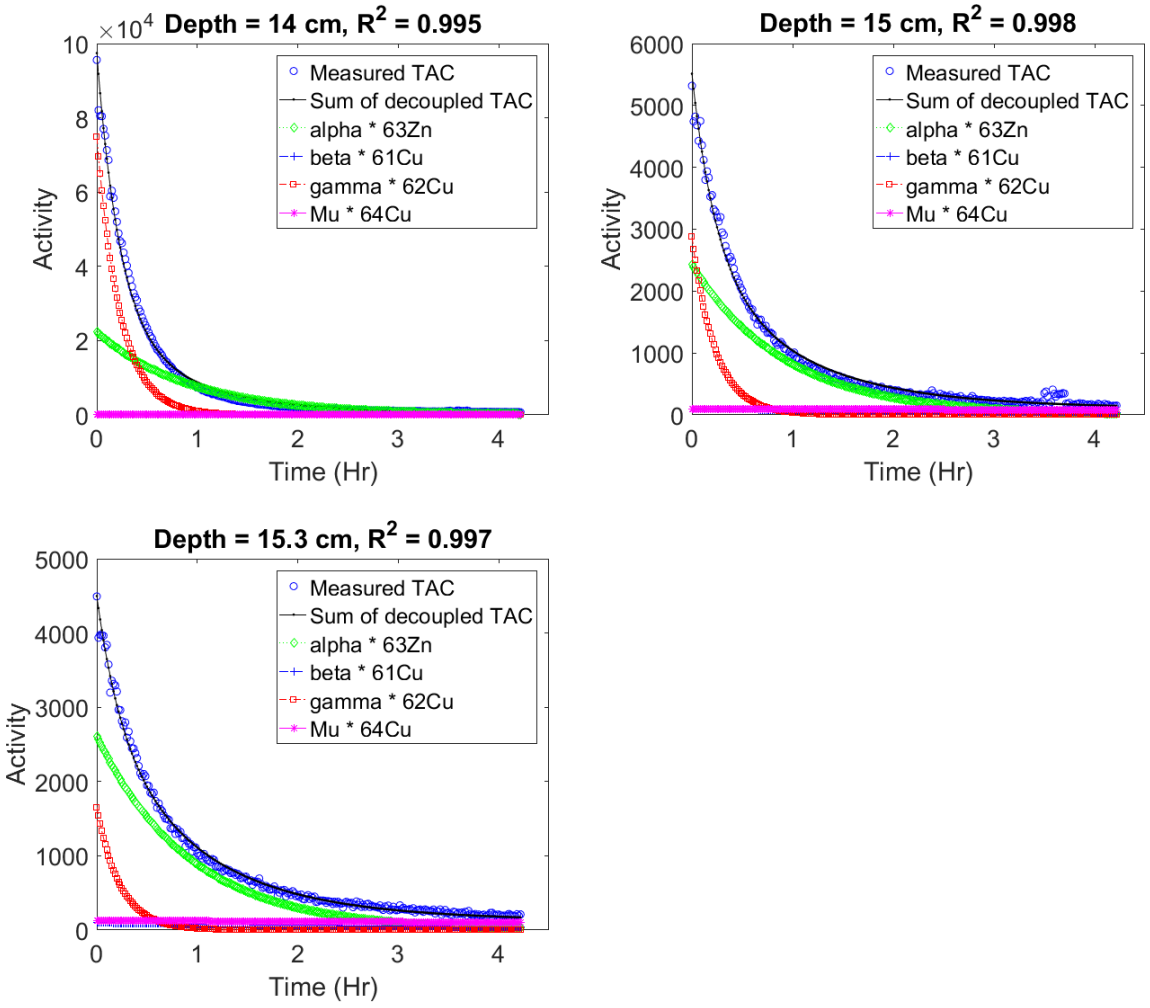

Figure 3.8. (a) Time activity curves (TAC) of progeny radioisotopes created by a monoenergetic beam. An iterative deconvolution method was used to separate the measured TAC into each radioisotope TAC. (b) Time activity curves (TAC) of progeny radioisotopes created by a SOBP beam.

3.7.2 Optimized Monoenergetic Spectra

Figures 3.9, 3.10 a) and 3.10 b) show the results of the optimized monoenergetic proton spectra. Using equation (3.7), the initial activities of each progeny radioisotope derived from the TAC curves in figure 3.8 (a) were used as input parameters to optimize the initial monoenergetic spectrum. Using equation (3.4), the initial spectra were estimated at depths of 14.0 cm, 15.0 cm, and 15.3 cm before optimization. In figure 3.9, the pre-optimized spectrum and optimized spectrum are plotted on the same axis. Both spectra were normalized to 1 and overlaid with the normalized nuclear interaction cross-sections. The FWHM (full width at half maximum) of our optimized spectra and Monte Carlo simulated spectra were compared. According to Figures 3.9, 3.10 a) and 3.10 b) the percentage differences of the FWHM of our optimized spectra compared to the MC simulated spectra at depths 14 cm, 15 cm and 15.3 cm were within 2 %.

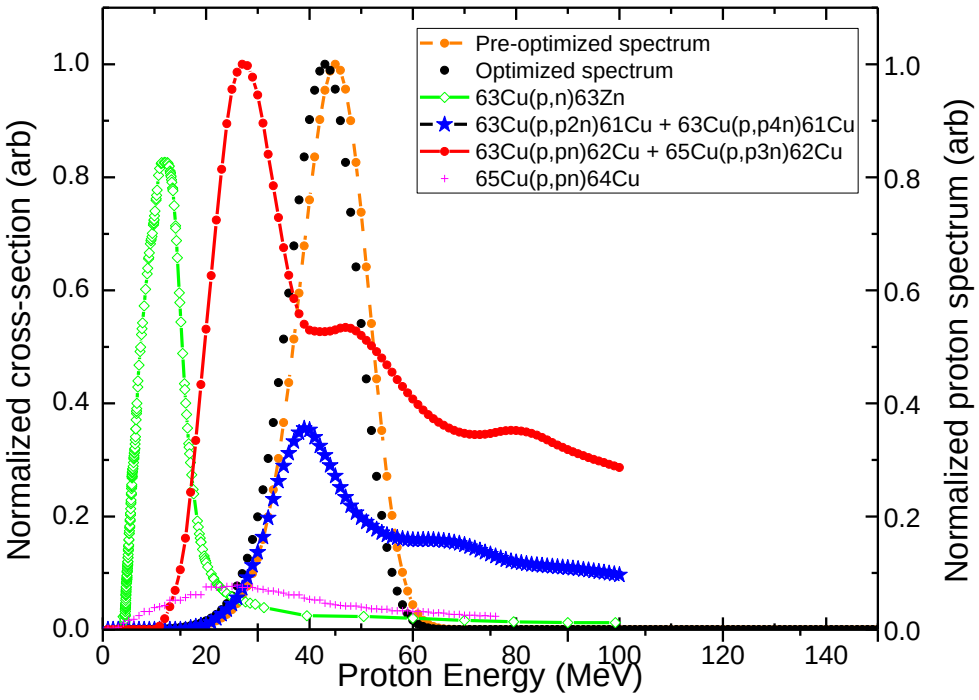

Figure 3.9. Comparison of optimized versus MC simulated spectrum for a monoenergetic beam at a depth of 14 cm in a water equivalent plastic phantom. The normalized nuclear interaction cross-sections are overlaid to show the positioning of the spectrum after optimization. We note that after optimization, the pre-optimized spectrum fits better with the simulated spectrum. There is a 2 % shift in the spectrum peak energy between the MC and optimized spectrum.

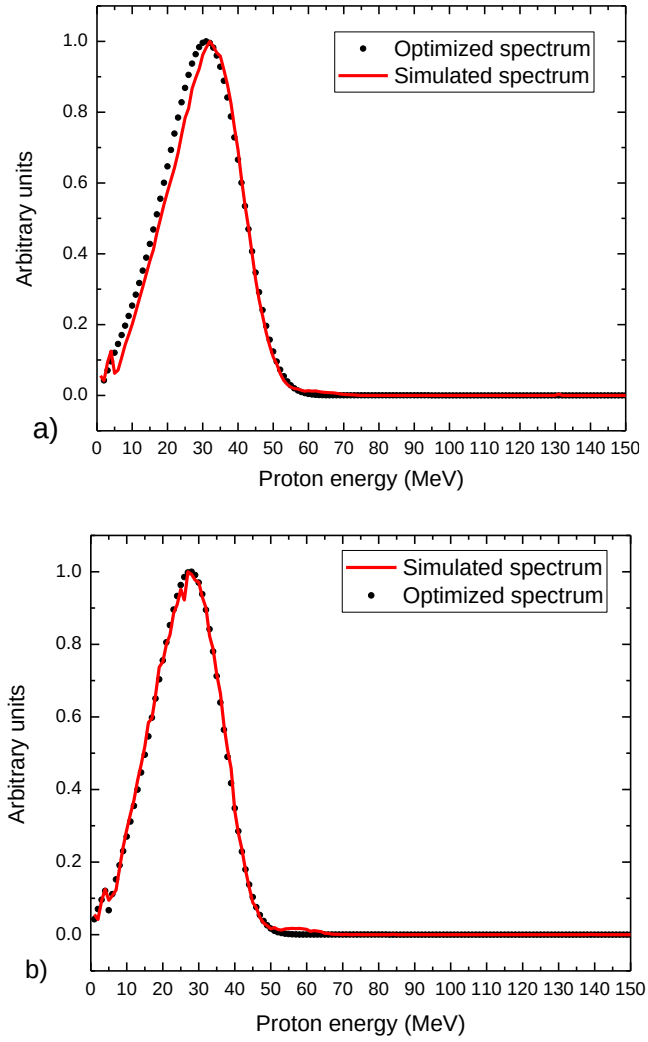

Figure 3.10. a) Comparison of optimized versus MC simulated spectrum for a monoenergetic beam at a depth of 15.0 cm in a water equivalent plastic phantom. (b) Illustrates the optimized versus MC simulated spectra at a depth of 15.3 cm in the phantom.

3.7.3 Optimized SOBP Spectra

Figure 3.11(a), (b) and (c) show the results of the optimized SOBP proton spectra. The pre-optimized SOBP spectra were estimated as shown in section 3.5, at depths of 14 cm, 15 cm , and 15.3 cm. According to figure 3.11(a), (b) and (c), The percentage deviation of the FWHM of our optimized spectra compared to the MC simulated spectra at depths 14 cm, 15 cm and 15.3 cm, were within 2%.

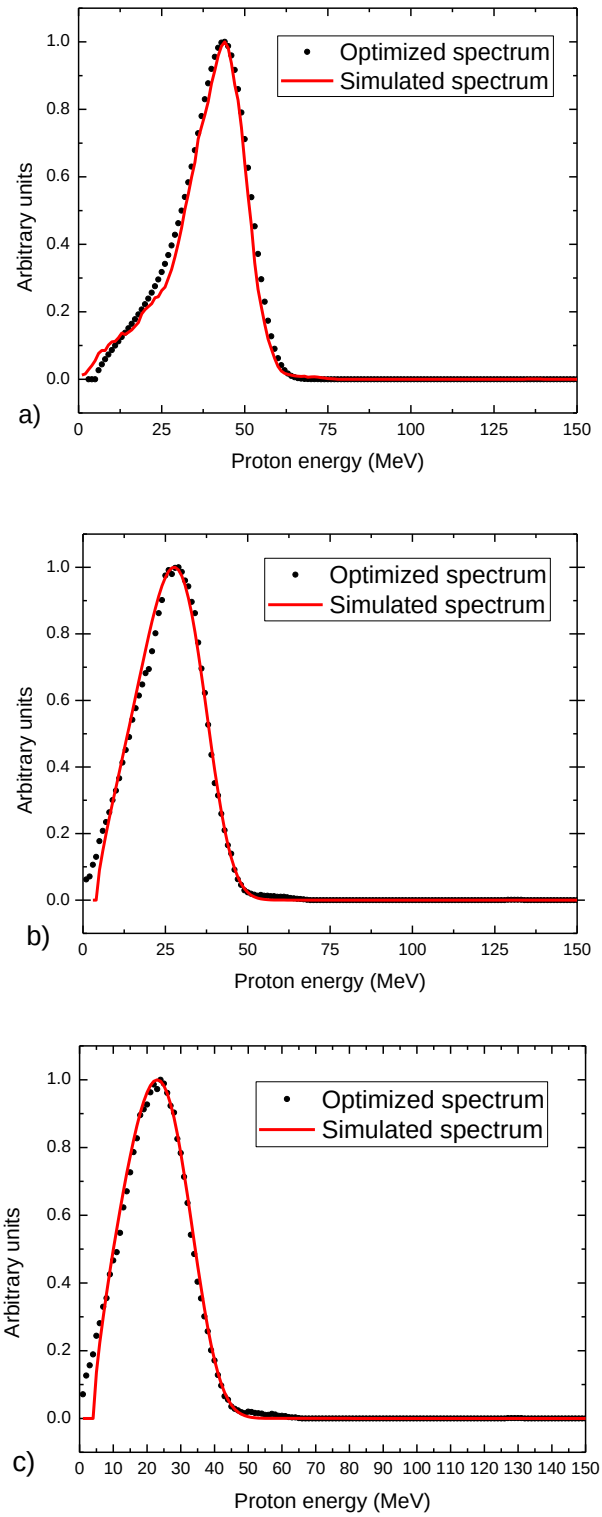

Figure 3.11. Comparison of optimized versus MC simulated spectrum for a SOBP beam at various depths in a water equivalent plastic phantom. a) At a depth of 14 cm, b) at a depth of 15 cm while (c) shows the optimized versus MC simulated spectra at a depth of 15.3 cm in the phantom.

Table 3.2. Comparison of the monoenergetic spectrum peak energy shifts between the optimized and MC simulated spectra at different depths in the phantom.

Depth in phantom (cm)	Optimized spectrum peak energy (MeV)	MC simulated spectrum peak energy (MeV)	Percentage deviation (%)
14	43	44	2.3
15	28	29	3.4
15.3	28	27	3.7

Table 3.3. Comparison of the SOBP spectrum peak energy shifts between the optimized and MC simulated spectra at different depths in the phantom.

Depth in phantom (cm)	Optimized spectrum peak energy (MeV)	MC simulated spectrum peak energy (MeV)	Percentage deviation (%)
14	44.4	44	0.9
15	29	28	3.5
15.3	24	23	4.3

Chapter 4

In this study, we test the feasibility of determining the proton beam range using a novel PG detection technique based on pair production. This method takes advantage of the high cross-section for pair production when high energy PG interacts with high Z materials like lead. High energy PG rays created in a hard water phantom during proton irradiation are intercepted by a lead slab. The PG rays interact by pair production with the nuclei of the lead slab resulting in the production of positron and electron pairs. The positrons rapidly annihilate with the surrounding electrons of the lead slab resulting in the emission of pairs of 511 keV annihilation gamma rays. The intensity of AG rays will scale with the intensity of emission of PG. Due to the high energies of the PG, the cross-section for pair production in lead is substantially greater than the cross-section for Compton interaction used in direct PG imaging methods such as Compton cameras. This should lead to a superior sensitivity of our novel PG detection method. We envision that the superior sensitivity of this method compared to other PG detection methods that directly measure the emitted PG rays using gamma detectors will improve proton range verification.

4.1 Theory of Prompt Gamma Emission

A nuclear inelastic collision of a proton with a target nucleus can leave the nucleus in an excited state (Cvijanovich et al., 1961, Szelecsényi et al., 1993). This is due to energy transfer from the incident protons to the target nucleus causing one or more nucleons to enter an excited state. The resultant de-excitation usually occurs in less than a few nanoseconds following the nuclear interaction, hence the name "*prompt*" gamma emission. The energy of the emitted PG ray depends on the target nucleus and the energy of the incident proton. Each isotope emits PG rays of a unique energy spectrum according to its nuclear energy levels.

The human body mass is composed 61.35% of oxygen and 22.8% of carbon (Emsley, 2011). When the body is irradiated with a proton beam, proton-induced nuclei interactions result in ^{12}C and ^{16}O nuclei excitation. These excited nuclei rapidly decay by emitting high energy PG, back to ground state. An example of this nuclear reaction is the emission of the 4.44 MeV PG resulting from proton-induced nuclear interaction with a ^{12}C nuclei, $^{12}C(p, p'\gamma^{4.44MeV})C^{12}$. Measuring these prompt gamma rays has been suggested as a potential method for proton range verification during proton treatment (Joost and Joao, 2014).

4.2 Prompt Gamma Ray Emission

The most significant PG ray emissions used in this study are from excited ^{12}C and ^{16}O (Verburg et al., 2013). The energy levels of these isotopes, excited states as shown by the energy level diagrams in figure 4.1. The significant reactions involving excited ^{16}O are: $^{16}O(p, p'\gamma^{2.74MeV})O^{16}$, $^{16}O(p, p'\gamma^{6.13MeV})O^{16}$, $^{16}O(p, p'\gamma^{6.92MeV})O^{16}$ and $^{16}O(p, p'\gamma^{7.12MeV})O^{16}$.

(Kozlovsky et al., 2002) shows the complete corresponding PG ray emission mechanisms after nuclear excitation of ^{12}C and ^{16}O nuclei.

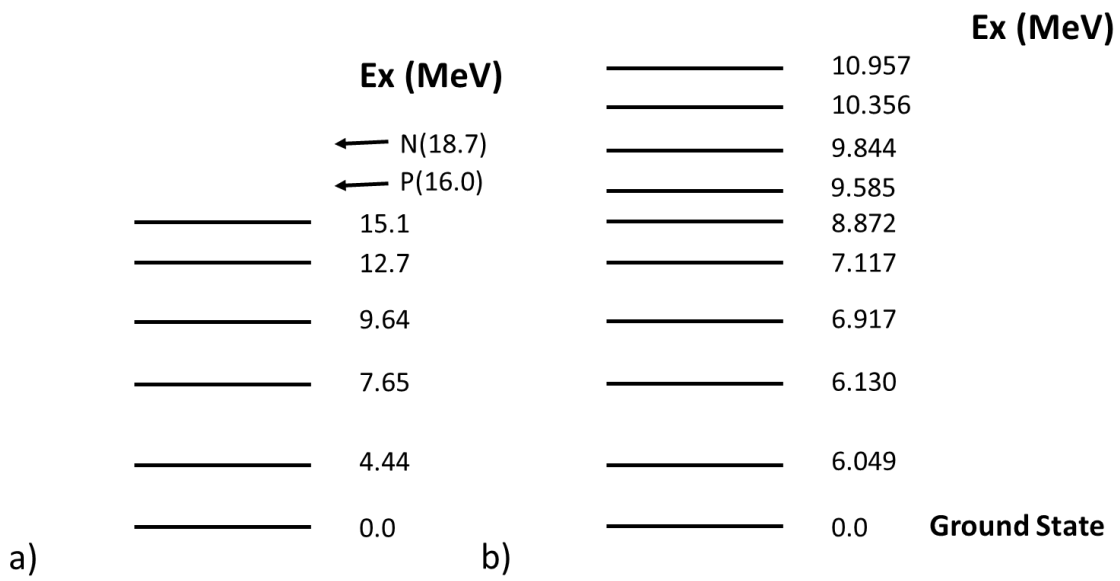

Figure 4.1. a) The energy level diagram for ^{12}C nucleus with its excited states (Aubrecht, 2003). b) Shows the energy level diagram for ^{16}O nucleus with its excited states. The right side axis shows the different energy levels in keV (J. Galt, 2005).

4.3 Number of Prompt Gamma Emissions per Incident Proton

The cross-sections for prompt gamma ray production in proton-induced nuclear reactions have been studied by several research groups including (Dyer et al., 1981, Kiener et al., 1998, Belhout et al., 2007, Lesko et al., 1988). As mentioned earlier, we based our study on the PG emissions due to proton-induced nuclear reactions on ^{12}C and ^{16}O. In this section, we estimate the maximum number of PG rays emitted per incident proton in a hard water phantom. The calculations were done using measured nuclear cross-section data for discrete gamma ray energies of 4.44 MeV from ^{12}C and 5.2 and 6.13 MeV from ^{16}O. These gamma ray energies were chosen because their emission correlates with the maximum rate of absorbed dose deposition in the Bragg peak. The average energy of the proton beam in the Bragg peak is ~14 MeV (residual range in water: 2 mm).

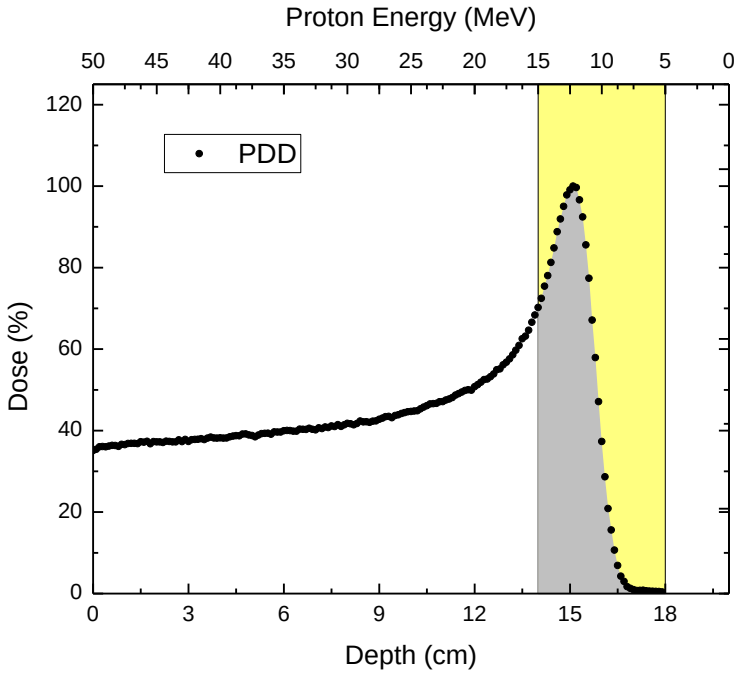

Figure 4.2. Percentage depth dose curve of a 150 MeV proton beam in a water phantom. The top x-axis was inverted to illustrate the correlation between the proton energy and the Bragg peak. The energy range where the intensity of PG emission is higher is illustrated by the shaded region.

The cross-sections for 4.44, 5.2 and 6.13 MeV PG emission are greatest between proton energies of 10 to 20 MeV and decrease sharply for higher proton energies (Dyer et al., 1981, Kiener et al., 1998). As shown in figure 4.2, the proton energy around the Bragg peak falls in this range. This explains the better correlation of the 4.44, 5.2 and 6.13 MeV PG emission with dose around the Bragg peak compared to positron emission. (Polf et al., 2014) carried out Monte Carlo simulations where they compared the dose deposited as an incident proton beam traversed a water phantom, to the 6.13 MeV PG emission intensity.

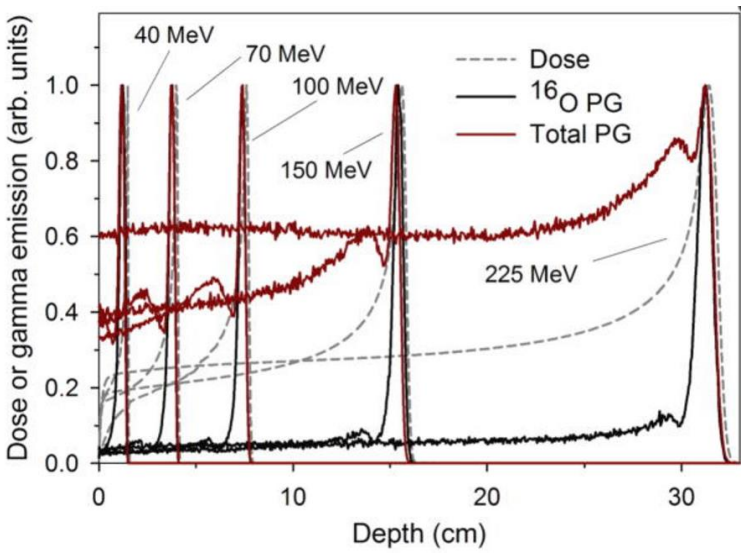

Figure 4.3. Comparison of dose, ^{16}O PG emission, and total gamma ray emission as a function of depth in a water phantom for proton beam energies 40, 70, 100, 150, and 225 MeV (Polf et al., 2014).

As shown in figure 4.3, there is a sharp peak in the 6.13 MeV PG emission intensity near the Bragg peak. The experimental nuclear cross-section for the discrete gamma rays 4.44, 5.2 and 6.13 MeV are shown in figures 4.4, 4.5, and 4.6.

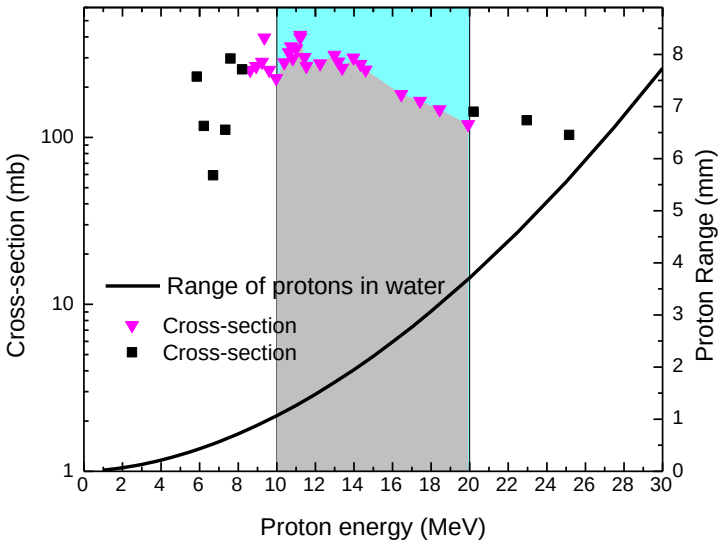

Figure 4.4. Experimental cross-section for the ^{12}C 4.44 MeV gamma ray emission as a function of proton energy (Belhout et al., 2007)&(Kiener et al., 1998).

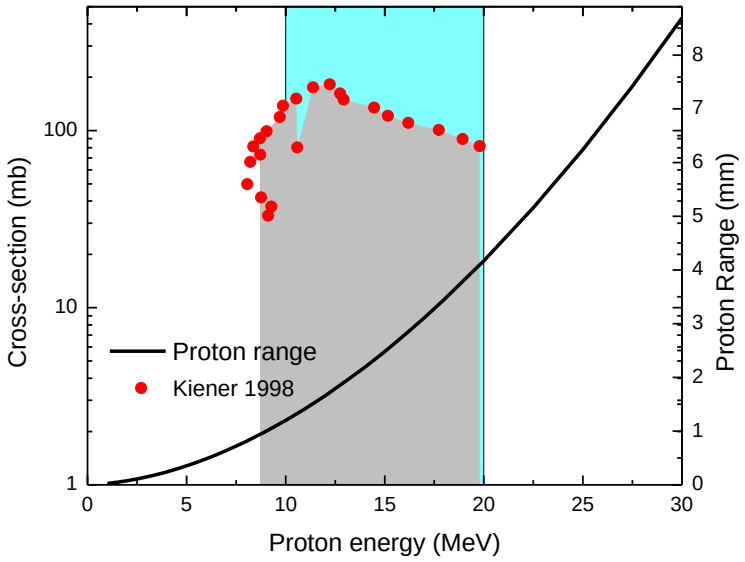

Figure 4.5.Experimental cross-section data for the ^{16}O 6.13 MeV gamma ray emission as a function of proton energy (Kiener et al., 1998).

The black line is a curve of the range of the proton energies on the x-axis. The shaded portion on both curves shows that the range of the protons for which the cross-sections for 4.44 and 6.13 MeV PG emission are greatest are from 1 to 4 mm.

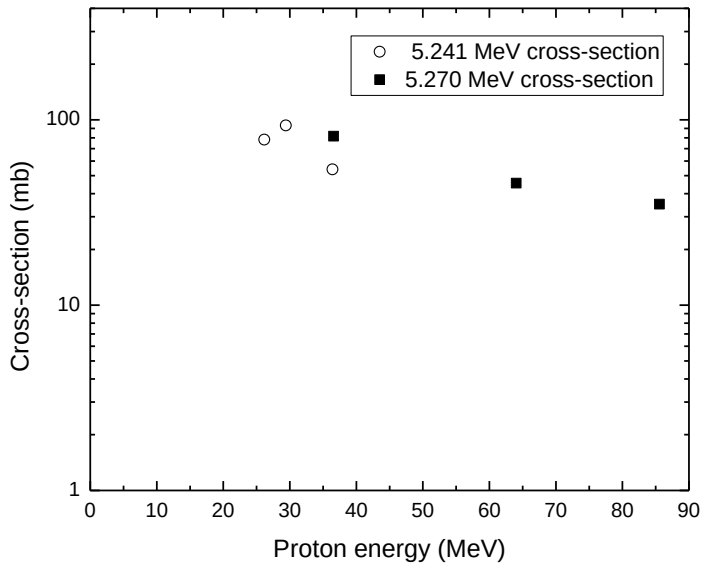

Figure 4.6.Gamma ray production cross-section measured by (Lesko et al., 1988) for the 5.241 and 5.247 MeV gamma ray emissions.

The number of detected prompt gamma rays, N_{PGs}, is given by:

$$N_{PGs} = \frac{N_{protons} dx \rho N_A \sigma}{A_W}$$

We determine the total number 4.44 and 6.13 MeV PG emitted by nuclear reactions in section 4.2 per incident proton from the sum of the probabilities of each interaction.

$$Total\ N_{PGs} = \sum \left[61.35\% \left(\frac{N_{protons} dx \rho N_A}{16} \right) \sigma_O(E) \right] + \sum \left[22.8\% \left(\frac{N_{protons} dx \rho N_A}{12} \right) \sigma_C(E) \right] \quad (2.1)$$

Where, ρ and dx are the water density and depth respectively, N_A is Avogadro's number, $\sigma_O(E)$ and $\sigma_C(E)$ are the nuclear cross-section for the 4.44 and 6.13 MeV PG emissions respectively. 61.35% and 22.8% are the percentage composition of Carbon and Oxygen in hard water respectively. From equation (2.1), the number of PG per incident proton per mm was found to be. $4.2 \times 10^{-4} \pm 7.1 \times 10^{-6}$. The uncertainty in this value is primarily from the cross-section measurements and the uncertainty in assuming a constant proton energy of 14 MeV. The number of PG per incident proton per mm that we calculated agrees within an order of magnitude with the results obtained from prompt gamma measurements by (Priegnitz et al., 2015). They used the IBA knife-edge slit camera and measured 4×10^{-4} emitted PG per protons per mm.

4.4 Probability of Pair Production in a Lead Slab

The probability of pair production in a lead slab depends on the energy of the incident photon, the thickness of the lead slab and its density. This is quantified by the mass *attenuation coefficient* for pair production in lead, i.e. the fraction of photons undergoing pair production in lead per area mass. The pair production mass attenuation coefficient for high-energy photons interacting with lead was obtained from the NIST XCOM database (Berger et al., 1999) and is shown in figure 4.7.

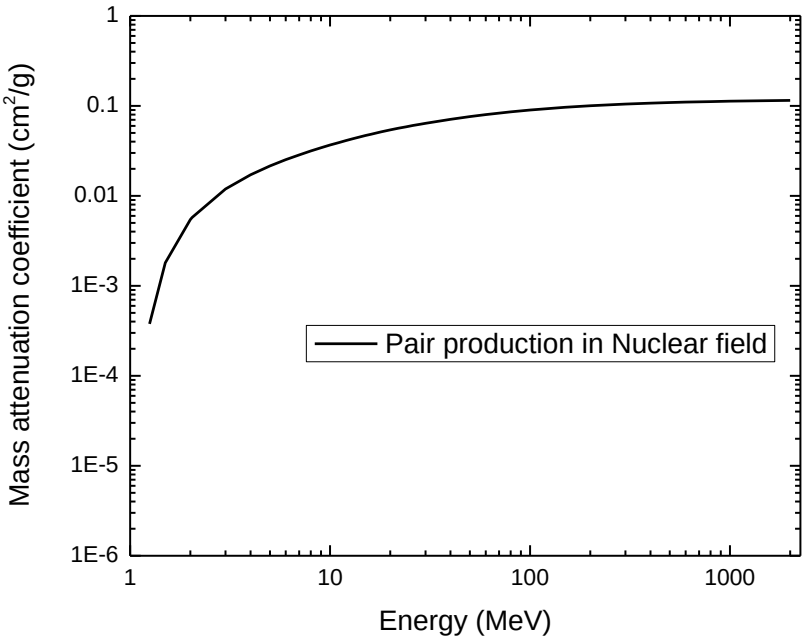

Figure 4.7. The pair production cross section in lead as a function of gamma ray energy.

Based on this figure, the probabilities of pair production for incident PG rays 4.44, 5.2 and 6.13 MeV on a 2.6 mm thin lead slab are approximately 2%, 2.5%, and 3.1%, respectively.

4.5 Materials and Methods

4.5.1 Monte Carlo Simulation

A Monte Carlo simulation of our proof of concept experiment was carried out for comparison purposes with our experimental results. The MC simulations were carried out with TOPAS (Tool For Particle Simulation), a GEANT 4 based software program (Agostinelli et al., 2003). The results of the Monte Carlo simulation were provided by (Cho, 2017). Corrections were made on the MC results for the difference in Geometry compared to the experimental results.

4.5.2 Experimental Setup

The goal of our proof of concept experiment was to demonstrate that the intensity of the emission of 511 keV AG produced by high energy PG rays from proton irradiation with C and O nuclei in a hard water phantom could be correlated with the position of the Bragg peak in the phantom

during proton irradiation. Figure 4.8 shows the setup used for this experiment. A 30 x 30 x 30 cm hard water phantom was irradiated with a 100 MU, 10 cm SOBP proton beam having a range of 15 cm (90 % dose) in water. Using a 10 cm thick lead block, prompt gamma radiation emitted from the phantom was collimated onto a 40 mm x 22 mm x 2.6 mm lead slab. These collimated prompt gammas interacted with the lead slab creating positron and electron pairs. Annihilation of the positrons with surrounding electrons in the lead slab results in 511 keV gamma rays emitted. Using a pair of lanthanum bromide (LBR) scintillation detectors, the AG rays are detected and their signal sent to a digitizer. The digitizer performed coincidence counting of the 511 keV gamma rays using a time resolution of 5 ns and energy window of ± 200 keV.

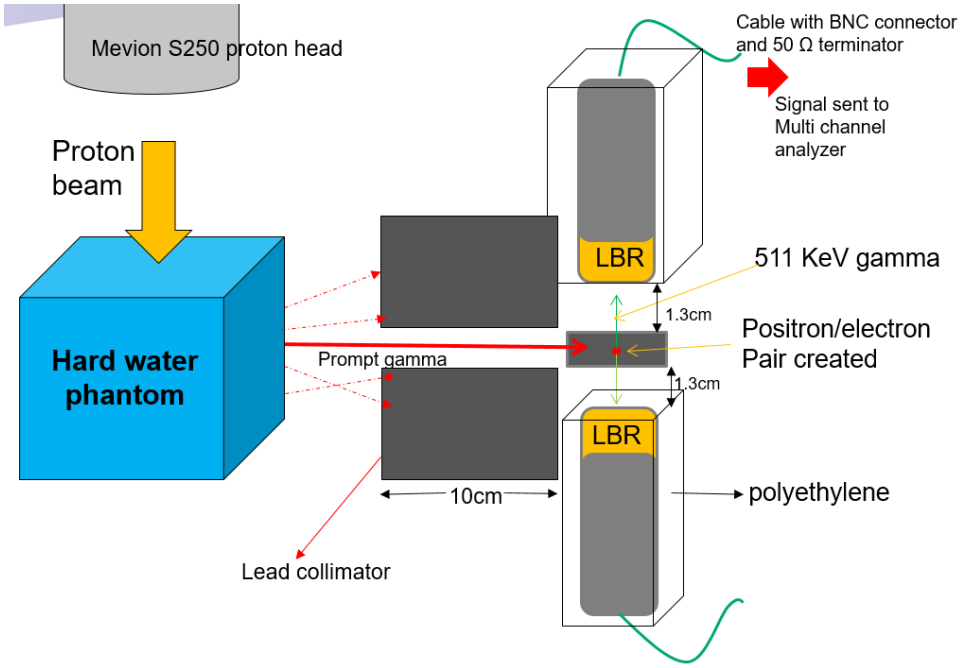

Figure 4.8. Experimental setup demonstrating proof of concept for the novel PG detection method. Upon proton irradiation of the phantom, PG emitted are collimated with the help of lead blocks onto a lead slab. 511 keV annihilation gammas rays emitted from the lead slab are measured using a pair of lanthanum bromide scintillation detectors.

4.5.3 Coincidence Detection Hardware and Software Development

AG rays from the thin lead slab were detected using a pair of LBR scintillation detectors. Voltage signals from the detector were sent to a National Instruments high-speed digitizer (HSD). The HSD used for this research was a model PXIe 5160 digitizer. The digitizer was driven using NI scope 15.1.1 software, with a maximum sampling rate of 2 GS/s and a bandwidth of 500 MHz. The signals from the PMT were fed into channels 0 and 1 of the digitizer. The NI scope software took the form of a Laboratory Virtual Instrument Engineering Workbench (LabVIEW) visual program. Maximum and minimum energy thresholds were set for the signals being digitized within LabVIEW. Signals above this amplitude threshold entering both channels were further analyzed. The difference in the amplitude and rise times of incoming signals within the required threshold can cause timing uncertainties. Because the coincidence timing for this study was done with a very small timing window, these uncertainties could affect the AG coincidence counting. A code was written in LabVIEW which deployed a constant fraction discrimination (CFD) technique to correct for this uncertainty. The CFD code separated the incoming signal into a pair of identical signals. One of the signals was inverted and delayed by 1 ns and added to the other signal as shown in figure 4.9.

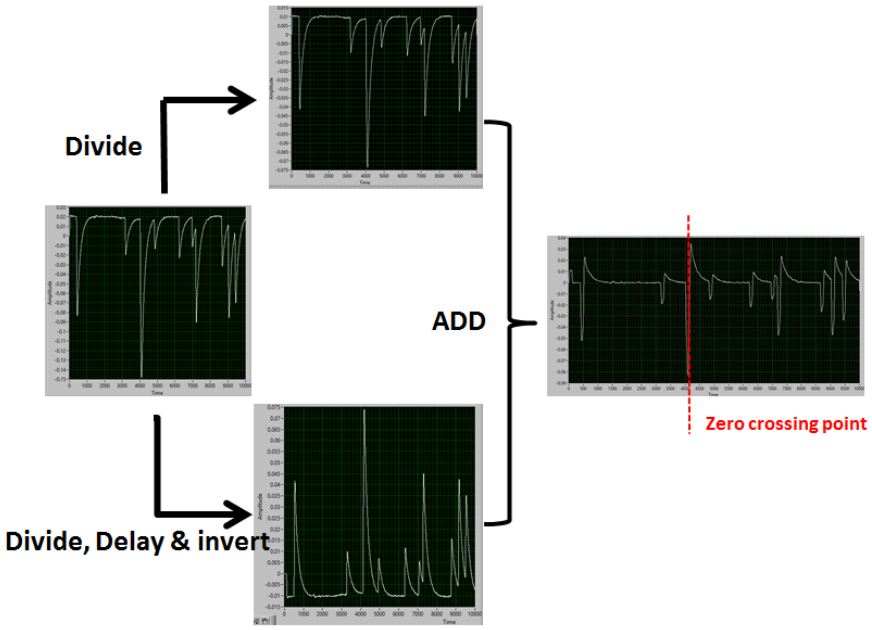

Figure 4.9. Results of constant fraction discrimination process in LabVIEW, for amplitude variability and timing correction.

The resultant signals from the CFD process were then processed by a code that performed the actual coincidence counting. The code compared the zero crossing points for signals from both channels and recorded a "1" each time the zero crossing points occurred within a 5 ns time window. The resultant number of counts after a complete analysis of the digitized signals represent the number of AG rays recorded by the LBR detector pair. The counts from the experimental setup were compared to the Monte Carlo simulation results. We tested this coincidence detection method by recording 511 keV gamma from a ^{22}Na check source. The check source had an activity of 0.8 µCi. Using our setup, we measured the activity of the check source and compared our results with the actual activity.

4.5.4 Principle of this Novel Prompt Gamma Detection Method

Our novel PG detection technique makes use of the following characteristics. The probability of pair production increases with increase in the atomic number of the target medium. The

attenuation coefficient for pair production is directly proportional to Z^2 of the target. Moreover, the probability of pair production increases with an increase in the incident photon energy. If prompt gamma rays emitted from a hard water phantom after nuclear reactions go on to penetrate a thin lead slab, these gamma rays can interact with the lead nuclei by pair production. The positrons ejected due to this interaction quickly annihilate with nearby electrons in the lead slab creating pairs of 511 keV AG rays. Each pair of AG ray is emitted simultaneously. By measuring AG emitted from the lead slabs during a small time window e.g. 5 ns the intensity of the AG ray counts can be recorded. This detection method is called fast coincidence detection. The AG counts can be correlated to the number of PG rays interacting with the lead slab. The intensity of PG emission correlates with the proton depth dose. Our method enables the indirect measurement of prompt gamma which can then be correlated with the proton depth dose profile to determine the range of the incident proton beam. In this chapter, I present proof of concept study of the results from this novel method, Monte Carlo simulations were carried and the resultant prompt gamma spectra from the simulation were measured. The profile of the simulated AG spectra is shown to correlate with the distal fall of region of the Bragg Peak.

4.5.5 Activation Gammas Emitted During Proton Beam Operation

The passive scatter proton delivery method results in the emission of gammas from proton and neutron activation of materials in the beam nozzle as the proton beam is scattered and collimated. The lead foil used for the first and second scattering can be activated and decay via gamma ray emission or emit neutrons when bombarded by protons. The graphite (^{12}C) used for range modulation can be a source of high-energy prompt gamma upon interactions with protons. Similarly, the brass wedge used to stop the beam and for collimation contains (55-65) % Cu and (35-45) % Zn. These elements have a high cross-section for nuclear interactions with high energy protons. Moreover, materials in the beam nozzle of the accelerator, consist of aluminum and other elements which can be activated by the proton beam. These materials can emit “background”

gamma rays that can affect the AG method of range verification. 511 keV gammas emitted from activated elements in the beam nozzle and patient for example can be detected along with those emanating the thin lead slab and thereby superimpose an unwanted signal on top of that resulting from PG formed inside the patient during irradiation. In order to access the "background" gamma ray environment in the treatment room during proton irradiation, the gamma ray energy spectrum was measured while the proton beam was operating.

4.5.6 Experimental Setup for Measuring the Gamma Ray Environment During Irradiation

Materials in the beam nozzle that help conform the dose to the treatment volume become radioactive from exposure to protons. The goal of this experiment was to measure and characterize the gamma environment in the proton treatment room when the proton beam was operating. A 30 x 30 x 30 cm hard water phantom was placed on a treatment table and with the use of the positioning lasers, centralized so that 200 cm SAD falls just beyond the proton range. A calibrated CANBERRA standard coaxial HPGe portable detector with (2' x 2') crystals was position in front of the phantom so that the midpoint of the phantom was at a distance of 50 cm from the detector as shown in figure 4.10. A MCA-8000A pocket multichannel analyzer (Amptek, Inc. Bedford, MA, USA) was connected to the HPGe detector. The MCA performed analog to digital conversion of the signals from the detector and grouped the signals into channels based on their pulse height which resulted in an energy spectrum. To be able to acquire the spectra during beam on, the MCA software had to be controlled from outside of the treatment room. This was done by using two laptops connected by a remote LAN connection.

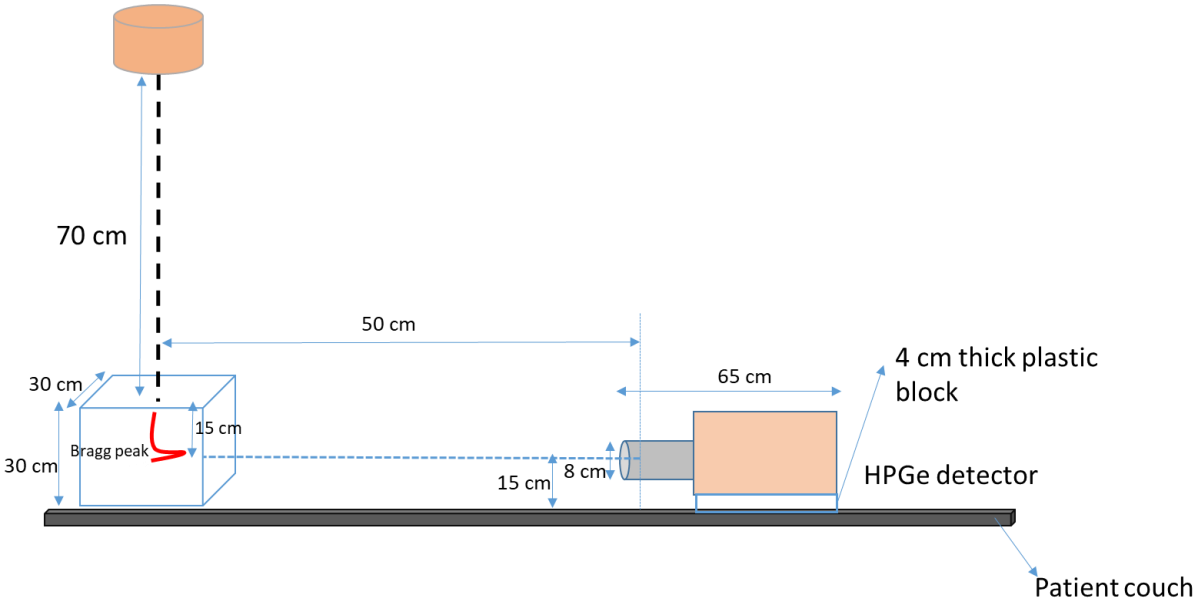

Figure 4.10. Experimental setup for measuring gammas emitted from proton activation and neutron capture reactions from the beam nozzle and hard water phantom

The phantom was irradiated with 100 MU of 150 MeV protons while simultaneously acquiring the gamma ray spectrum using the HPGe detector. Measurements were made at two different gain settings, a gain of 30 on the pulse shaping amplifier was used in order to obtain high-resolution gamma ray spectra at the lower end of the spectrum, e.g. < 1000 keV. A gain of 3 on the pulse shaping amplifier was used to measure the whole of the spectrum up to a maximum of 6000 keV.

The low energy spectrum was seen to smear out due to pulse pile-up when the detector was at a distance of 50 cm from the phantom. A higher quality spectrum at low energy was obtained when the detector was at a distance of 100 cm. Due to the small cross-section for photoelectric effect at higher energies (i.e. energies where Compton scattering and pair production dominate), the high energy spectra were measured with the detector at a distance of only 50 cm from the phantom.

4.6 Results and Discussion

4.6.1 Monte Carlo Simulation of Prompt Gamma Spectra

The simulation of a 150 MeV monoenergetic spectrum consisting of 10^7 protons bombarding the water phantom, resulted in the emission of 4.14 x 10^5 prompt gammas (decay time < 10 ns). Figure 4.11 shows the prompt gamma spectrum emitted from the water phantom as generated by the MC simulation (Cho, 2017).

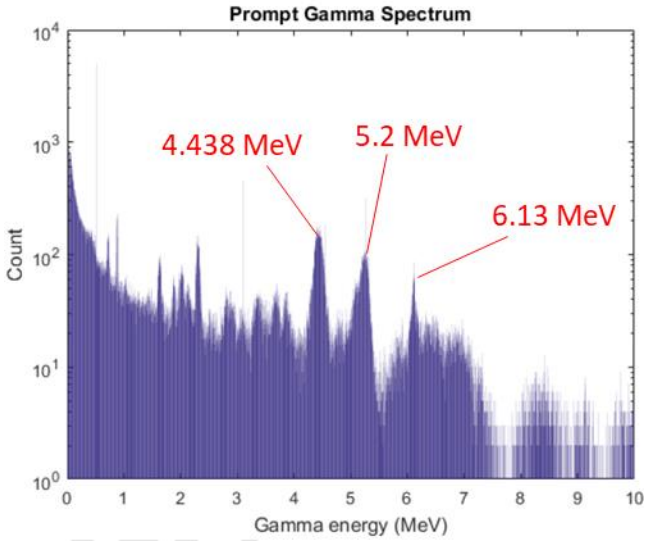

Figure 4.11. The spectrum of prompt gammas (< 10 ns decay time) emanating from the water phantom. Gamma peaks around 4.4 MeV and 6.1 MeV are from excited carbon and oxygen, respectively.

4.6.2 Proton Range Verification Results

The MC simulation of this novel proton range verification method yielded positive preliminary results. figure 4.12 shows the relative magnitude of prompt gamma-induced AG produced by the lead pair production target in the simulation. This means that the prompt gammas emitted at each depth created positron and electron pairs in the 1 mm x 25 mm lead ring located at each depth. The peak of the AG counts visually lines up quite closely with the Bragg peak.

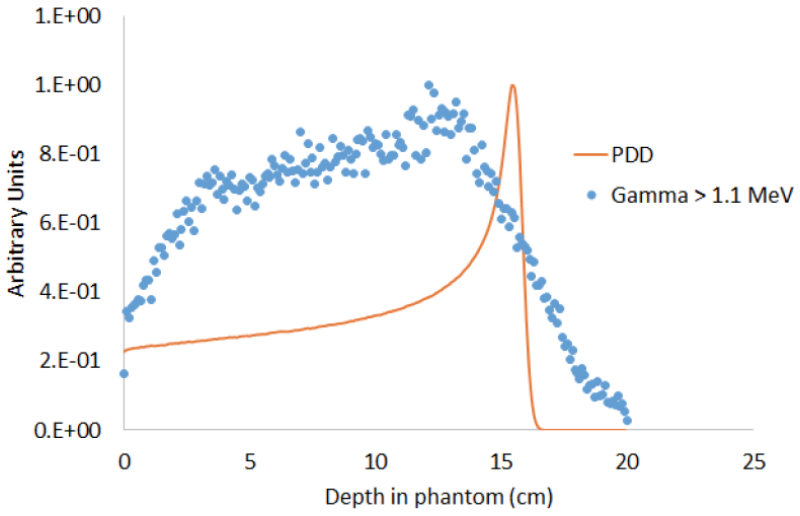

Figure 4.12. The relative magnitude of prompt gamma-induced AG. The maximum amount of prompt gamma rays are emitted approximately 2 cm proximal to the Bragg-Peak depth and decreases rapidly beyond the Bragg-peak depth.

We compared the spectra of AG gamma counts simulated with two different time coincidence windows, ±0.5 ns and ±5 ns using an energy window 511 ± 0 keV. Figure 4.13 shows a negligible difference (<1 %) between both spectra.

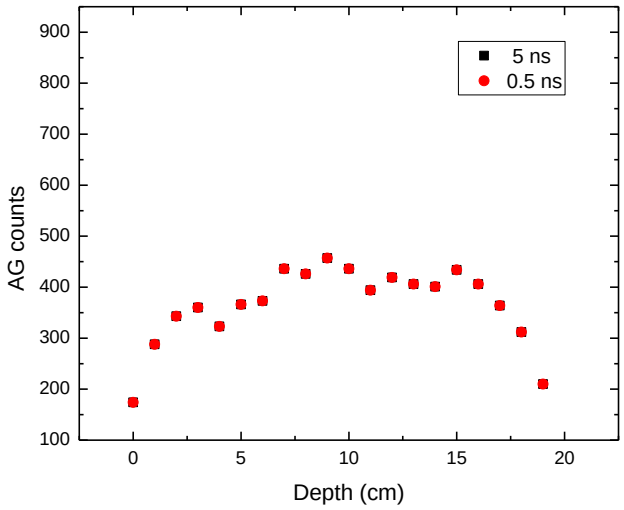

Figure 4.13. MC simulated annihilation gamma depth profile at 20 different depths in the water phantom. The AG depth profile is directly proportional to the prompt gamma spectrum.

AG counting simulation with a coincidence window of ± 20 ns and energy window 511±200 keV was compared to the AG spectrum generated with the ± 0.5 ns / 511± 0 keV coincidence and energy windows as shown in figure 4.14.

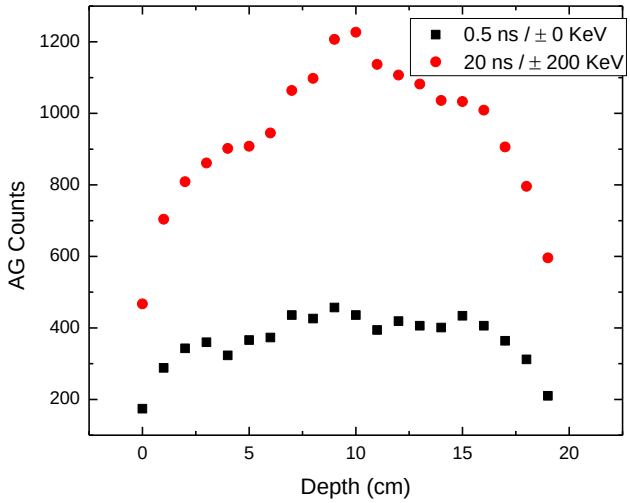

Figure 4.14. Annihilation gamma spectrum simulated with a time coincidence window of 0.5 ns and energy window of ± 0 keV compared to the spectrum simulated with a time coincidence window of 20 ns and energy window of ±200 keV

The number of AG counts from the 20 ns/ 511±200 keV simulation increased by approximately 200 % compared to the 0.5 ns/ 511 ± 0 keV simulated AG counts for each lead ring. This increase is likely due to the larger energy window permitting more coincidence counts. Normalizing both spectra to 1 and overlaying with the Percentage depth dose curve used for the simulation yields figure 4.15.

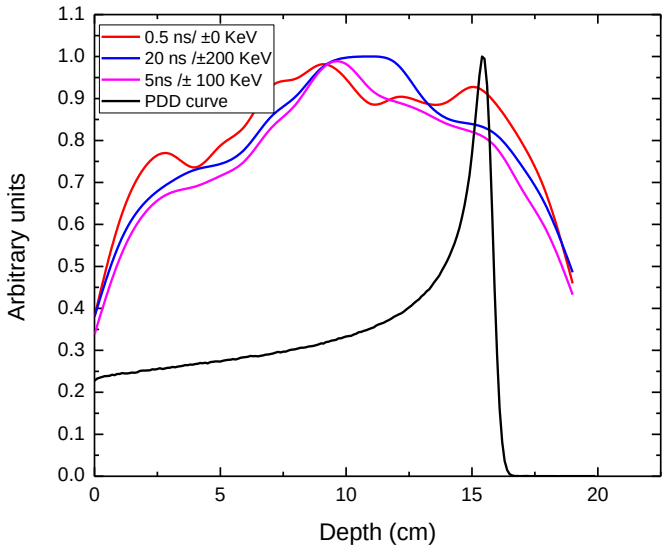

Figure 4.15. Normalized annihilation gamma spectra overlaid with the PDD of the proton beam used for this simulation. The rather bumpy nature of the spectra is because not enough histories (10^6) was used for the Monte Carlo simulation.

4.6.3 Comparison of Experimental and Simulated Results

The average number of AG counts or Prompt gamma counts recorded from the Monte Carlo simulation between depths of 10 cm and 15 cm was approximately 10000 PG/s. This number was obtained after correcting for difference in geometry between the MC simulation and experimental setup. Using the same time coincidence window as in the MC simulation, 5 ns and energy window 511 ± 200 keV, we recorded ~ 300 PG/s counts from our experimental setup as shown in table 4.1.

Table 4.1. Comparison of our experimental and Monte Carlo simulated prompt gamma counts recorded with a time coincidence window of 5 ns and energy window ± 200 keV. The number in parenthesis is MS results multiplied by the detector efficiency (12 %).

	Energy Window	Coincidence time window	Approximate PG counts per second
Monte Carlo simulated	511 ± 200 keV	5 ns	10000 (1200)
Measured	511 ± 200 keV	5 ns	300

The MC simulations results were roughly 30 times greater than the measured results. Our coincidence detectors were estimated to have approximately 12 % efficiency due to detection efficiency and geometric considerations. Multiplying this efficiency by the simulated PG counts resulted in a better agreement with the measured results as shown in table 4.1. Table 4.2 below shows the results of our Monte Carlo simulation compared to results from a similar PG experiment using the IBA gamma slit knife edge camera (Smeets et al., 2012). The minimum PG counts per proton per mm from our simulation was obtained using time coincidence and energy window combination 0.5 ns/ 511 ± 0 keV while the maximum PG counts per proton and mm was measured using a time coincidence and energy window combination 20 ns/ 511 ± 200 keV. Comparing with the results by (Priegnitz et al., 2015) using the same parameters, our system proved to be quite superior with a sensitivity ∼10 times greater table 4.2.

Table 4.2. Comparison of our novel AG, PG detection method scaled to IBA method detection parameters.

	AG method	IBA Compton camera (Priegnitz et al., 2015)
Axis of beam to collimator front distance	23 cm	23 cm
Axis of beam to detector distance	33 cm	45 cm
Emitted gammas per protons and mm	3.5×10^{-4}	4×10^{-4}
Counts per proton per 1 mm	Minimum of 8×10^{-6} per 4 mm	8×10^{-7} per 4 mm (average)
	Maximum of 2.4×10^{-5} per 4 mm	1.2×10^{-6} per 4 mm (maximum)

4.6.4 Gamma Ray Spectrum During Proton Irradiation

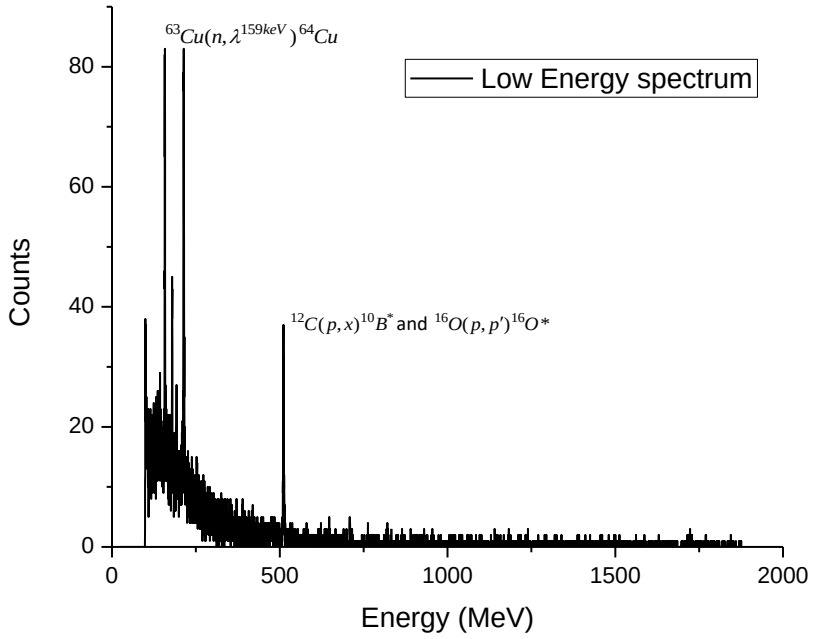

Figure 4.16. The spectrum of low energy gammas emitted from the proton beam nozzle after proton activation and neutron capture reactions. The phantom was irradiated with 100 MU and the detector placed 100 cm from the hard phantom.

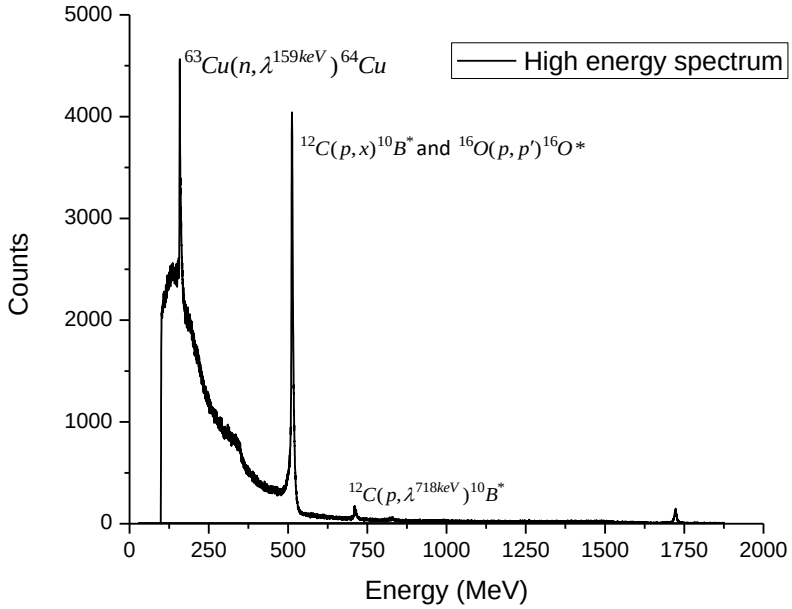

Figure 4.17. The spectrum of High energy gammas emitted from the proton beam nozzle after proton activation and neutron capture reactions. The phantom was irradiated with 1000 MU protons and the detector placed 50 cm from the hard phantom.

Figure 4.16 shows the low energy gamma peaks emitted from the proton beam nozzle. We believe that the 159 keV peak shown in figure 4.17 is the result of the fast neutron capture reaction $^{63}Cu(n,\gamma^{159keV})^{64}Cu$, with the copper in the brass wedge. This gamma ray is emitted with a nuclear cross-section of 0.648 barns. The 511 keV peak results from several proton activation reactions with elements along the beam path in the nozzle including: $^{63}Cu(p,pn)^{62}Cu$ and $^{68}Zn(p,2n)^{67}Ga$. The decay of proton activated ^{12}C and ^{16}O through reactions $^{12}C(p,x)^{10}B^{*}$ and $^{16}O(p,p')^{16}O*$, respectively in the hard water phantom are the sources emitting the highest counts of 511 keV AG. We believe that the 718 keV peak is as a result of proton activation reaction with the graphite scatterers which are made up of carbon 12 i.e. $^{12}C(p,\lambda^{718keV})^{10}B^{*}$.

Chapter 5

Conclusion and Discussion

5.1 Peak Energy Determination Conclusions and Discussions

For the first project, we presented a new method for determining the peak energy of a proton energy spectrum. The performance of our coincidence detector setup proved to be accurate. An initial test of our coincidence detector was done using a 0.8 μCi 22Na check source. This radioisotope decayed by positron emission. 511 keV annihilation gamma was detected using our system and after correcting for angular dependence and detector efficiency, we recorded the activity of the check source. The measured activity using our system had a good agreement compared to the calculated activity.

Our results demonstrated that this approach is valid i.e. we can determine what the peak energy is at a particular depth in a Bragg Peak. The percentage deviation of our optimized spectra compared to the MC simulated spectra were acceptable. As shown in figure 3.9, the peak energy of the pre-optimized monoenergetic spectrum shifted after our method was implemented and better matched the MC simulated spectrum. Also, a quantitative evaluation was performed using the Chi-squared method. There was a good agreement between our optimized spectra and Monte Carlo simulated spectra (Chi-square alpha of 0.05 (level of significance)). The behavior of our optimized spectrum with increasing depth was acceptable. There was a broadening and decrease in amplitude with depth as expected as shown in figure 3.4.

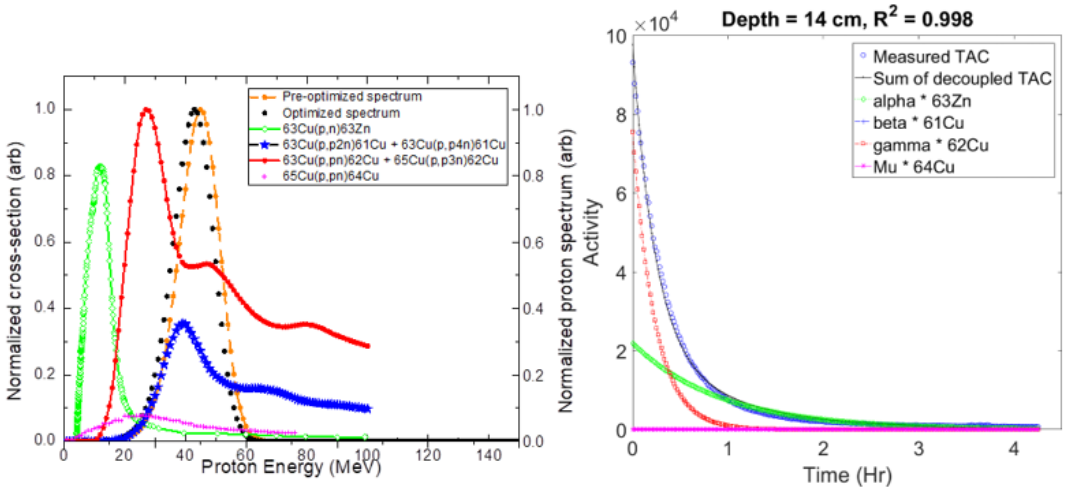

Figure 5.1. Graphs showing the relationship between the activity of each progeny radioisotope and their nuclear cross-sections, to the position of the monoenergetic proton spectrum on the energy axis. The left graph shows the optimized monoenergetic spectrum at a depth of 14 cm in water.

As shown in figure 5.1, it should be noted that the overlap area under the spectrum and nuclear-cross-section are directly proportional to the relative activity of each progeny radioisotope. For the optimized monoenergetic proton spectrum at a depth of 14 cm, the overlap region under the proton spectrum and the ^{62}Cu cross-section curve is the greatest. Looking at the TAC curve for monoenergetic beams at depth 14 cm, the relative activity of ^{62}Cu is also the greatest. Similarly, the overlap region under the proton spectrum and the ^{64}Cu is small. This is consistent with the low activity of ^{64}Cu when the Cu foil was irradiated at a depth of 14 cm. The percentage deviation of the FWHM of our optimized spectra compared to the MC simulated spectra at depths 14 cm, 15 cm and 15.3 cm, were within 2%. While the proton peak energy for the SOBP spectra at depths 14 cm, 15 cm, and 15.3 cm were within 4% deviation from the MC simulated spectra, which is quite acceptable, and demonstrate that this method of proton energy peak determination is worth pursuing.

The proposed method can be used for proton spectrum peak energy measurements in a clinical setting with either time-coincidence detectors or a conventional PET scanner. These measurements could provide information on the energy of the proton beam around the Bragg peak. Its simplicity and ease of replication make it feasible to be used as a validation for Monte Carlo simulated spectra. The proposed method may shift the Monte Carlo simulation validation procedure from physical dose comparisons to energy spectra comparisons, which will provide more confidence in RBE calculation.

Future work is underway, to further optimize this method. Uncertainty propagation resulting from both cross-section uncertainties and uncertainties in the detection of AG resulting from each created radioisotope following Cu activation would be carried out. A set of much more precise experiments can be carried out with copper foils placed at more positions. This will give us many more activity values to be used to optimize the proton peak energy, resulting in a more accurate value.

5.2 Novel Proton Range Verification Method Conclusions and Discussions

Prompt gamma imaging has been suggested as a technique for *in vivo* proton dose and range verification after proton induced-tissue activation. During irradiation, activated tissue decay within less than 4 nanoseconds emitting high-energy prompt gammas. In this chapter, we assessed the feasibility of using pair production interaction of the emitted high energy PG on a lead slab as an *in vivo* proton range verification method. This was done by measuring 511 keV annihilation gamma rays emitted when the positrons annihilated with surrounding electrons in the lead slab.

This study was based on imaging mainly the 4.44 MeV gamma line from ^{12}C activation and the 5.2 and 6.13 MeV emitted gamma lines from ^{16}O. The cross-sections for 4.44, 5.2 and 6.13 MeV PG emission are greatest between proton energies of 10 to 20 MeV. These proton

energies have ranges 1- 4 mm in water. As shown in figure 4.2, the Bragg peak occurs within these proton energy ranges. This proves that, PG ray detection can be used to infer the position of the Bragg peak, or proton range within 1- 4 mm of accuracy. A crude hand calculation was done in section 4.3 to estimate the total number of prompt gamma of these energies emitted per incident proton. This calculation was based on several assumptions. Firstly, because the cross-section for emission of PG of these energies is very low for incident proton particles of energy greater than 30 MeV, the calculation above this 30 MeV were ignored. After solving, we obtained a value of $4.2 \times 10^{-4} \pm 7.1 \times 10^{-6}$ PG per incident proton per mm which was approximately within an order of magnitude similar to the results 4×10^{-4} PG per incident proton per mm obtained from measurements by (Priegnitz et al., 2015). Our Monte Carlo simulation resulted in approximately 2.3×10^{-4} PG per protons per mm. Using the XCOM database the probability of pair production for incident photons on a 1mm thin lead slab was calculated. Approximately 2%, 2.5% and 3.1% probability of pair production on the 2.6 mm lead slab for incident photons of energies 4.44 MeV, 5.2 MeV and 6.13 MeV gamma rays respectively were calculated. Due to the high cross-section for pair production for this higher energy PG rays, the sensitivity of our detection method was quite good. As shown in table 4.2, our system is ~10 times more sensitive in comparison to the IBA camera. Keeping in mind that these results were obtained from a Monte Carlo simulation, these results would vary for actual measurements with the introduction of geometric and detector efficiencies and other measurement uncertainties.

The proof of concept experiment involved placing a lead slab at a distance from a hard water phantom, irradiating the phantom with a proton beam and intercepting the prompt gamma emitted from the phantom with the lead slab. The absorbed PG rays interact with the lead slab through pair production which resulted in the emission of AG rays. A fast coincidence detection system was built to measure the emitted AG rays using a pair of LBR scintillation detectors and an NI digitizer. Preliminary results of the PG count from the simulation and measurement setup

were quite promising. By matching the simulation setup to the experimental setup while using the same time coincidence and energy windows, the measured PG counts deviated from the MC simulation PG counts by ~30 %. This deviation can be as low as ~4% considering detection efficiencies.

Proton activation of materials along the beam path in the nozzle results in the emission of low energy gammas as the created radioisotopes decay. Also, neutrons knocked out from the scatterers could undergo neutron capture reactions to emit low energy gammas. Due to the high flux of the proton beam, the emission of low energy activation gammas during irradiation could result in a lot of false AG counting when using our detection method. These reactions also result in 511 keV gamma emission which might affect our range verification results. A possible solution for this is better shielding the detection setup from the activation gammas. To achieve this, a knowledge of the gamma environment in the treatment room during beam on is important. We measured the gamma spectrum after irradiating the hard water phantom used in this study. After irradiating the phantom, the emitted gamma spectra from the proton beam nozzle and phantom were measured. We noticed a high count of 511 keV gamma peaks possibly resulting from reactions $^{63}Cu(p,pn)^{62}Cu$, $^{68}Zn(p,2n)^{67}Ga$, $^{12}C(p,x)^{10}B^{*}$ and $^{16}O(p,p')^{16}O*$. One of the significant energy peaks was the 718 keV peak from the carbon 12 activation reaction $^{12}C(p,x)^{10}B^{*}$. The energy peak information from the measured spectra can be used to develop appropriate shielding for our novel prompt gamma detection method.

Suggestions for further research include, using pulse shaping amplifiers to amplify the signals emanating from the lead slab. This will help reduce pulse pile-up which is a major concern for this method because of the high-energy PG also hitting the detector. Moreover, higher fidelity MC simulation with the same dimensions as the experimental setup would provide a better knowledge of the sensitivity and accuracy of this method.

5.3 Concluding statement

In this thesis, we used measured time activity curves from proton activated copper foils to estimate the peak energy of both monoenergetic and SOBP proton spectra. We also presented a novel proton range verification method based on prompt gamma imaging. The proposed method setup must be shielded from background gamma to avoid false coincidence 511 keV gamma counts. So, the gamma environment in the proton treatment room was characterized to provide information required for shielding the setup. All specific aims have been accomplished throughout this research and this concludes the thesis.

REFERENCES

AGOSTINELLI, S., ALLISON, J., AMAKO, K. A., APOSTOLAKIS, J., ARAUJO, H., ARCE, P., ASAI, M., AXEN, D., BANERJEE, S. & BARRAND, G. 2003. GEANT4—a simulation toolkit. *Nuclear instruments and methods in physics research section A: Accelerators, Spectrometers, Detectors and Associated Equipment,* 506**,** 250-303.

AUBRECHT, G. 2003. A teachers guide to the nuclear science wall chart. *Contemporary Physics Education Project*.

BELHOUT, A., KIENER, J., COC, A., DUPRAT, J., ENGRAND, C., FITOUSSI, C., GOUNELLE, M., LEFEBVRE-SCHUHL, A., DE SÉRÉVILLE, N. & TATISCHEFF, V. 2007. γ-ray production by proton and α-particle induced reactions on C 12, O 16, Mg 24, and Fe. *Physical Review C,* 76**,** 034607.

BENTON, E. 2016. Nuclear Interactions, Reactions, and Collions. *PHYS 4663*.

BENTON, E. & FRANK, A. 2002. Passive dosimetry aboard the Mir Orbital Station: internal measurements. *Radiation measurements,* 35**,** 439-455.

BERGER, M. J., HUBBELL, J. H., SELTZER, S. M., COURSEY, J. S. & ZUCKER, D. S. 1999. XCOM: Photon cross section database (version 1.2). *http://physics. nist. gov/xcom*.

CHADWICK, M., OBLOŽINSKÝ, P., HERMAN, M., GREENE, N., MCKNIGHT, R., SMITH, D., YOUNG, P., MACFARLANE, R., HALE, G. & FRANKLE, S. 2006. ENDF/B-VII. 0: next generation evaluated nuclear data library for nuclear science and technology. *Nuclear data sheets,* 107**,** 2931-3060.

CHERRY, S. R., SORENSON, J. A. & PHELPS, M. E. 2012. *Physics in Nuclear Medicine E-Book,* London, UNITED STATES, Elsevier Health Sciences.

CHO, J. 2017. Private Communication.

CHO, J., IBBOTT, G., GILLIN, M., GONZALEZ-LEPERA, C., MIN, C. H., ZHU, X., EL FAKHRI, G., PAGANETTI, H. & MAWLAWI, O. 2013. Determination of elemental tissue composition following proton treatment using positron emission tomography. *Physics in medicine and biology,* 58**,** 3815.

CHRISTIAN, G., FERNANDO, H.-G., ANDREAS, M., PETER, D., WOLFGANG, E., FINE, F., THOMAS, K., KATJA, R., JOHANNES, P., ANDREAS, W. & GUNTRAM, P. 2014. Range assessment in particle therapy based on prompt γ -ray timing measurements. *Physics in Medicine & Biology,* 59**,** 5399.

CVIJANOVICH, G., DAYTON, B., EGLI, P., KLAIBER, B., KOCH, W., NIKOLIĆ, M., SCHNEEBERGER, R., WINZELER, H., COMBE, J. C., GIBSON, W. M., LOCK, W. O., SCHNEEBERGER, M. & VANDERHAEGHE, G. 1961. Nuclear excitation and multiple production in proton-nucleon collisions at CERN-PS energies. *Il Nuovo Cimento (1955-1965),* 20**,** 1012-1016.

DYER, P., BODANSKY, D., SEAMSTER, A. G., NORMAN, E. B. & MAXSON, D. R. 1981. Cross sections relevant to gamma-ray astronomy: Proton induced reactions. *Physical Review C,* 23**,** 1865-1882.

EMSLEY, J. 2011. *Nature's building blocks: an AZ guide to the elements*, Oxford University Press.

FOURKAL, E., VELCHEV, I., FAN, J., LUO, W. & MA, C.-M. 2007. Energy optimization procedure for treatment planning with laser-accelerated protons. *Medical physics,* 34**,** 577-584.

GHOSHAL, S. N. 1950. An Experimental Verification of the Theory of Compound Nucleus. *Physical Review,* 80**,** 939-942.

GRANVILLE, D. A. & SAWAKUCHI, G. O. 2015. Comparison of linear energy transfer scoring techniques in Monte Carlo simulations of proton beams. *Physics in medicine and biology,* 60**,** N283.

HALL, E. J., ASTOR, M., BEDFORD, J., BOREK, C., CURTIS, S. B., FRY, M., GEARD, C., HEI, T., MITCHELL, J. & OLEINICK, N. 1988. Basic radiobiology. *American journal of clinical oncology,* 11**,** 220-252.

HAYAT, M. J., HOWLADER, N., REICHMAN, M. E. & EDWARDS, B. K. 2007. Cancer Statistics, Trends, and Multiple Primary Cancer Analyses from the Surveillance, Epidemiology, and End Results (SEER) Program. *The Oncologist,* 12**,** 20-37.

HOFFMANN, W., MOLLER, G., BLATTMANN, H. & SALZMANN, M. 1980. Pion dosimetry with thermoluminescent materials. *Physics in medicine and biology,* 25**,** 913.

HUANG, S., CARSON, A., HOFFMAN, E. & PHELPS, D. K. E. 1982. An Investigationof a Doubleâ€" TracerTchniquefor PositronComputerized Tomography. *J Nucl Med,* 23**,** 816-822.

HUESO-GONZÁLEZ, F., GOLNIK, C., BERTHEL, M., DREYER, A., ENGHARDT, W., FIEDLER, F., HEIDEL, K., KORMOLL, T., ROHLING, H., SCHÖNE, S., SCHWENGNER, R., WAGNER, A. & PAUSCH, G. 2014. Test of Compton camera components for prompt gamma imaging at the ELBE bremsstrahlung beam. *Journal of Instrumentation,* 9**,** P05002.

JOHNS, H. & CUNNINGHAM, J. 1983. The physics of radiology 4th ed. *Thomas Springfield, Illinois*.

JOOST , M. V. & JOAO, S. 2014. Proton range verification through prompt gamma-ray spectroscopy. *Physics in Medicine & Biology,* 59**,** 7089.

KHAN, F. M. & GIBBONS, J. P. 2014. *Khan's the physics of radiation therapy*, Lippincott Williams & Wilkins.

KIENER, J., BERHEIDE, M., ACHOURI, N., BOUGHRARA, A., COC, A., LEFEBVRE, A., DE OLIVEIRA SANTOS, F. & VIEU, C. 1998. γ-ray production by inelastic proton scattering on 16 O and 12 C. *Physical Review C,* 58**,** 2174.

KORMOLL, T., FIEDLER, F., SCHÖNE, S., WÜSTEMANN, J., ZUBER, K. & ENGHARDT, W. 2011. A Compton imager for in-vivo dosimetry of proton beams—A design study. *Nuclear Instruments and Methods in Physics Research Section A: Accelerators, Spectrometers, Detectors and Associated Equipment,* 626**,** 114-119.

KOZLOVSKY, B., MURPHY, R. J. & RAMATY, R. 2002. Nuclear deexcitation gamma-ray lines from accelerated particle interactions. *The Astrophysical Journal Supplement Series,* 141**,** 523.

KRANE, K. S. 1988. *Introductory nuclear physics* New York : Wiley.

LESKO, K., NORMAN, E., LARIMER, R.-M., KUHN, S., MEEKHOF, D., CRANE, S. & BUSSELL, H. 1988. Measurements of cross sections relevant to γ-ray line astronomy. *Physical Review C,* 37**,** 1808.

LEVKOVSKIJ 1991. Cross-sections of medium mass nuclides activation (A=40–100) by medium energy protons and alpha particles (E=10–50). *Inter-Vesi.*

LITZENBERG, D., ROBERTS, D., LEE, M., PHAM, K., VANDER MOLEN, A., RONNINGEN, R. & BECCHETTI, F. 1999. On-line monitoring of radiotherapy beams: Experimental results with proton beams. *Medical physics,* 26**,** 992-1006.

MAURO, T., CHUL HEE, M., JOOST , M. V., JAN, S., HSIAO-MING, L. & HARALD, P. 2014. Range verification of passively scattered proton beams based on prompt gamma time patterns. *Physics in Medicine & Biology,* 59**,** 4181.

MEADOWS, J. W. 1953. Excitation Functions for Proton-Induced Reactions with Copper. *Physical Review,* 91**,** 885-889.

MIN, C.-H., KIM, C. H., YOUN, M.-Y. & KIM, J.-W. 2006. Prompt gamma measurements for locating the dose falloff region in the proton therapy. *Applied physics letters,* 89**,** 183517.

MOTEABBED, M., ESPAÑA, S. & PAGANETTI, H. 2011. Monte Carlo patient study on the comparison of prompt gamma and PET imaging for range verification in proton therapy. *Physics in Medicine & Biology,* 56**,** 1063.

NICHOLS, A. L., SINGH, B. & TULI, J. K. 2012. Nuclear Data Sheets for A = 62. *Nuclear Data Sheets,* 113**,** 973-1114.

NISHIO, T., MIYATAKE, A., INOUE, K., GOMI-MIYAGISHI, T., KOHNO, R., KAMEOKA, S., NAKAGAWA, K. & OGINO, T. 2008. Experimental verification of proton beam monitoring in a human body by use of activity image of positron-emitting nuclei generated by nuclear fragmentation reaction. *Radiological Physics and Technology,* 1**,** 44-54.

NISHIO, T., SATO, T., KITAMURA, H., MURAKAMI, K. & OGINO, T. 2005. Distributions of β+ decayed nuclei generated in the CH2 and H2O targets by the target nuclear fragment reaction using therapeutic MONO and SOBP proton beam. *Medical Physics,* 32**,** 1070-1082.

PAGANETTI, H. 1998. Monte Carlo method to study the proton fluence for treatment planning. *Medical physics,* 25**,** 2370-2375.

PAGANETTI, H., NIEMIERKO, A., ANCUKIEWICZ, M., GERWECK, L. E., GOITEIN, M., LOEFFLER, J. S. & SUIT, H. D. 2002. Relative biological effectiveness (RBE) values for proton beam therapy. *International Journal of Radiation Oncology* Biology* Physics,* 53**,** 407-421.

PARODI, K., PAGANETTI, H., SHIH, H. A., MICHAUD, S., LOEFFLER, J. S., DELANEY, T. F., LIEBSCH, N. J., MUNZENRIDER, J. E., FISCHMAN, A. J. & KNOPF, A. 2007. Patient study of in vivo verification of beam delivery and range, using positron emission tomography and computed tomography imaging after proton therapy. *International Journal of Radiation Oncology* Biology* Physics,* 68**,** 920-934.

POLF, J., PETERSON, S., MCCLESKEY, M., ROEDER, B., SPIRIDON, A., BEDDAR, S. & TRACHE, L. 2009. Measurement and calculation of characteristic prompt gamma ray spectra emitted during proton irradiation. *Physics in medicine and biology,* 54**,** N519.

POLF, J. C., MACKIN, D., LEE, E., AVERY, S. & BEDDAR, S. 2014. Detecting prompt gamma emission during proton therapy: the effects of detector size and distance from the patient. *Physics in medicine and biology,* 59**,** 2325-2340.

PRIEGNITZ, M., HELMBRECHT, S., JANSSENS, G., PERALI, I., SMEETS, J., VANDER STAPPEN, F., STERPIN, E. & FIEDLER, F. 2015. Measurement of prompt gamma profiles in inhomogeneous targets with a knife-edge slit camera during proton irradiation. *Physics in medicine and biology,* 60**,** 4849.

PRUSATOR, M., AHMAD, S. & CHEN, Y. 2017. TOPAS Simulation of the Mevion S250 compact proton therapy unit. *Journal of Applied Clinical Medical Physics,* 18**,** 88-95.

RUTHERFORD, E. 1911. LXXIX. The scattering of α and β particles by matter and the structure of the atom. *The London, Edinburgh, and Dublin Philosophical Magazine and Journal of Science,* 21**,** 669-688.

SAWAKUCHI, G. O., SAHOO, N., GASPARIAN, P. B., RODRIGUEZ, M. G., ARCHAMBAULT, L., TITT, U. & YUKIHARA, E. G. 2010. Determination of average LET of therapeutic proton beams using Al2O3: C optically stimulated luminescence (OSL) detectors. *Physics in medicine and biology,* 55**,** 4963.

SMEETS, J., ROELLINGHOFF, F., PRIEELS, D., STICHELBAUT, F., BENILOV, A., BUSCA, P., FIORINI, C., PELOSO, R., BASILAVECCHIA, M., FRIZZI, T., DEHAES, J. C. & DUBUS, A. 2012. Prompt

gamma imaging with a slit camera for real-time range control in proton therapy. *Physics in Medicine & Biology,* 57**,** 3371.

SZELECSÉNYI, F., BLESSING, G. & QAIM, S. M. 1993. Excitation functions of proton induced nuclear reactions on enriched 61Ni and 64Ni: Possibility of production of no-carrier-added 61Cu and 64Cu at a small cyclotron. *Applied Radiation and Isotopes,* 44**,** 575-580.

TAVERNIER, S. 2010. *Experimental techniques in nuclear and particle physics*, Springer Science & Business Media.

VERBURG, J. M., RILEY, K., BORTFELD, T. & SECO, J. 2013. Energy-and time-resolved detection of prompt gamma-rays for proton range verification. *Physics in medicine and biology,* 58**,** L37.

WILSON, R. R. 1946. Radiological use of fast protons. *Radiology,* 47**,** 487-491.

VITA

Percy Forsuh Nebah

Candidate for the Degree of

Master of Science

Thesis: OPTIMIZATION OF PROTON THERAPY BY ESTIMATION OF THERAPEUTIC PROTON SPECTRUM AND VERIFICATION OF PROTON RANGE

Major Field: Physics

Biographical:

Education:

Completed the requirements for the Master of Science in Physics at Oklahoma State University, Stillwater, Oklahoma in December, 2017.

Completed the requirements for the Bachelor of Engineering with an emphasis in medical physics from Carl Von Ossietzky University Oldenburg, Germany in 2014.

Experience:

Undergraduate research assistant, Pius Hospital Oldenburg, Germany 2013 - 2014; Graduate Research assistant, Oklahoma state University, Stillwater, Ok, 2015 – 2017;

Professional Memberships:

The American Association of Physicists in Medicine (AAPM)